



Tectonothermal evolution of a collisional orogen in the Khammam region, southeastern India: insights from structures, phase equilibria modeling and U–Th–(total) Pb monazite geochronology

H. Hrushikesh^{1,2} · Praveen C. Singh¹ · N. Prabhakar¹ · Sachin K. Thakur¹ · Bidisha Dey^{1,3}

Received: 2 June 2020 / Accepted: 7 October 2020 / Published online: 11 November 2020
© Springer-Verlag GmbH Germany, part of Springer Nature 2020

Abstract

The Khammam Schist Belt (KSB), southeastern India, represents a part of the collision zone that is sandwiched between the Eastern Dharwar Craton to the west and the Eastern Ghats Mobile Belt (EGMB) to the east. Quartzofeldspathic gneisses of the EGMB and garnet–kyanite metapelites of the KSB have been investigated to characterize P – T – t evolution of the Khammam region. Pseudosection modeling reveals that the melt-bearing quartzofeldspathic gneiss experienced peak and post-peak metamorphism at P – T conditions of 7.9–8.1 kbar/790–810 °C and ~7.0 kbar/740–750 °C, respectively. In contrast, metapelite witnessed peak metamorphism at 7.4–7.8 kbar/600–640 °C, followed by post-peak retrogression at 6.1–6.6 kbar/590–625 °C. U–Th–(total) Pb monazite ages from the gneiss constrain the peak and retrograde metamorphic episodes at 1.63–1.53 Ga and 1.48–1.38 Ga, while those in the metapelites were determined at 1.25–1.20 Ga and 1.18–1.10 Ga, respectively. These P – T – t estimates indicate that the KSB, Vinjamuru, and Ongole domains evolved distinctly during Late Paleoproterozoic–Late Mesoproterozoic. The younger ages (0.90–0.81 Ga) were ascribed to the formation of the Eastern Indian Tectonic Zone, implying its extension beyond the western margin of the EGMB. Besides, the distinct Neoproterozoic ages (2.79–2.45 Ga) are related to the Archean protolith of the quartzofeldspathic gneisses, which were likely derived from the Archean crust of the Napier–Rayner Complex. This tectonothermal restoration is new and characterizes the Khammam region as the hot and composite collision zone with protracted geological history. (250 words)

Keywords Southeastern India · Garnet · P – T – t evolution · Monazite geochronology · Collision orogen · East Antarctica

Introduction

The tectonic configuration of collision zones is thought to be a product of long-lived accretion between distinct continental blocks in which crustal domains develop complex deformation structures and metamorphic history (Harris et al. 1994; Brown et al. 2006). Based on the following observations, such an intercontinental collision zone undoubtedly provides critical constraints on understanding the geodynamic behavior of accreted crustal fragments during the collision process. First, the lithodemic units in the collision zone preserve vital information about their deformation and metamorphism during burial and exhumation processes (Vernon 1978; Norris et al. 1990; Jamieson et al. 2002). The application of in situ geochronology on these lithologies (e.g., U–Th–(total) Pb monazite dating; Suzuki and Adachi 1991; Montel et al. 1996; Williams and Jercinovic 2002) provides better insights into the tectono-metamorphic evolution of polydeformed

Communicated by Daniela Rubatto.

Electronic supplementary material The online version of this article (<https://doi.org/10.1007/s00410-020-01744-7>) contains supplementary material, which is available to authorized users.

✉ N. Prabhakar
prabhakarnaraga@gmail.com; prabhakarnaraga@iitb.ac.in

- ¹ Department of Earth Sciences, Indian Institute of Technology Bombay, Powai, Mumbai 400076, India
- ² Present Address: State Unit: Assam, North Eastern Region, Geological Survey of India, Guwahati 781005, India
- ³ Present Address: Department of Earth and Planetary Systems Science, Hiroshima University, Hiroshima 739-8526, Japan

crustal provinces (e.g., England and Thompson 1984; Zhao and Cawood 1999). Second, detailed accretion-related tectonic processes documented from the collision zone have been proven essential prerequisite for reconstructing dispersed crustal blocks within supercontinent assembly (e.g., Kluth and Coney 1981; Beaumont et al. 1996; Cawood and Buchan 2007; Zhuang et al. 2015).

The Khammam Schist Belt (KSB), a part of the Proterozoic collision zone in southeastern India, is sandwiched between the Eastern Dharwar Craton (EDC) and the Eastern Ghats Mobile Belt (EGMB) (Fig. 1a; Ramam and Murty 1997; Hari Prasad et al. 1999; Okudaira et al. 2001). The belt is a collage of imbricated metasedimentary sequences that were accreted to the eastern margin of the EDC (Ramam and Murty 1997; Saha 2002). During this accretion and cratonization, the lithologies of the KSB and neighboring domains have been affected by multiple episodes of syn- to post-collisional

deformation and metamorphism. These tectonic activities indicate that the belt preserves a protracted accretionary history along the eastern boundary of the EDC (Hari Prasad et al. 2000). A previous metamorphic study from the KSB amphibolites has identified peak P - T conditions of 8–12 kbar and 650–750 °C, which reveals the evidence for high- T metamorphism in the belt (Hari Prasad et al. 2000). The timing of this high-grade metamorphic event was determined at 824 ± 43 Ma using Sm–Nd mineral isochron (Okudaira et al. 2001). According to Hari Prasad et al. (2000), the KSB could represent a terrane evolved in an oceanic or continental margin island arc setting. However, these petrological and geochronological studies on the KSB were mostly retrieved from amphibolites and provide limited information on the pressure (P)–temperature (T)–time (t) history of the KSB. As a result, the tectonic evolution of the accretionary system in and around the KSB remains unclear. Therefore, a

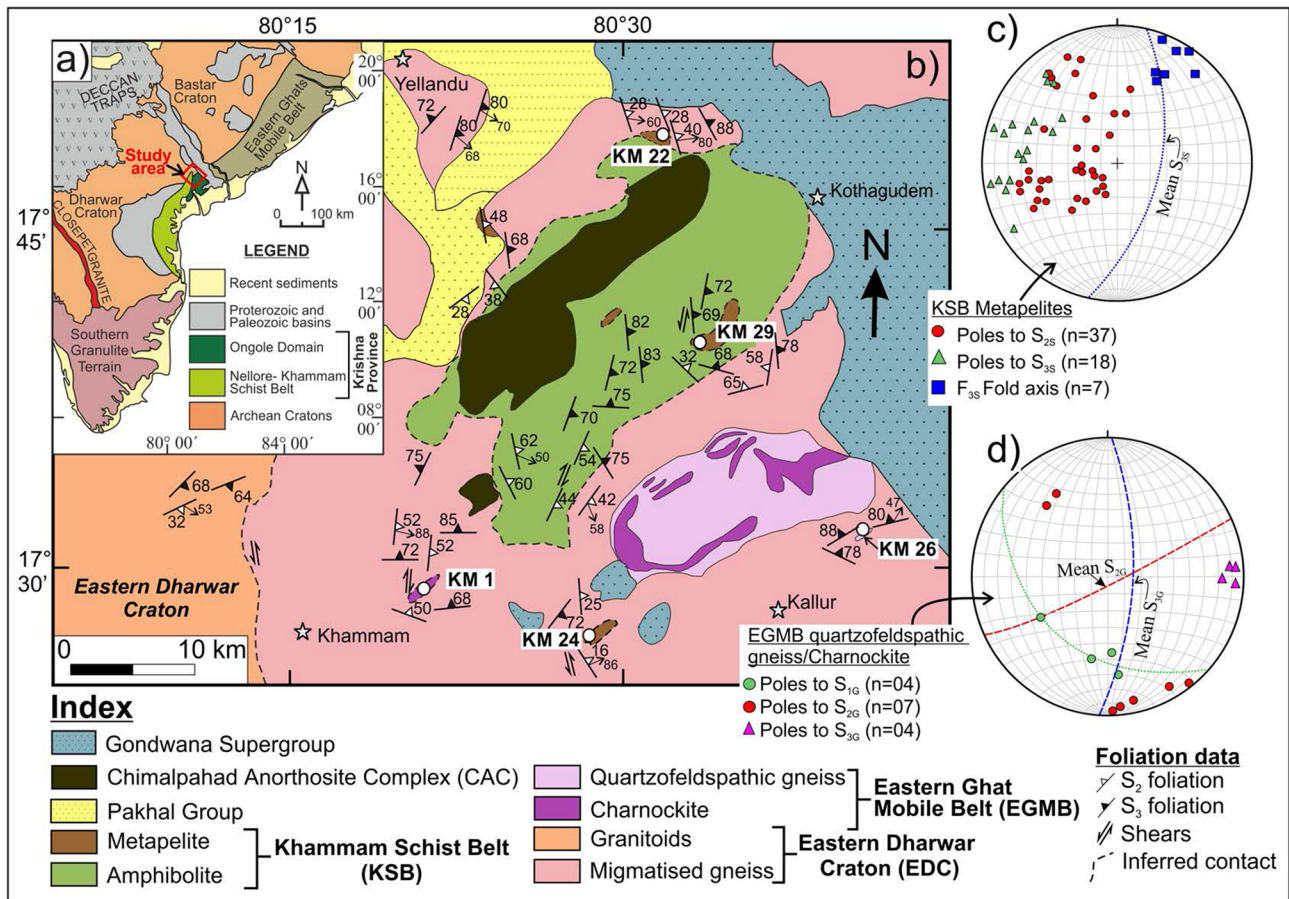


Fig. 1 a Simplified tectonic map of central and southern India showing the distribution of major Archean cratons and Proterozoic mobile belts (modified after Narayanaswami 1966). The box represents the location of the Khammam region in southeastern India. **b** Generalized geological map of the Khammam region showing different lithological units with mesoscopic foliation patterns. Locations of the samples used for P - T estimation (KM-24, 29, and 26C) and monazite dating (KM-26C and 29) are also shown on the map. Equal-area projections show a summary of linear and planar data obtained from **c** metapelites of the KSB and **d** quartzofeldspathic gneisses of the EGMB

tions of the samples used for P - T estimation (KM-24, 29, and 26C) and monazite dating (KM-26C and 29) are also shown on the map. Equal-area projections show a summary of linear and planar data obtained from **c** metapelites of the KSB and **d** quartzofeldspathic gneisses of the EGMB

multidisciplinary approach that integrates structures and phase equilibria modeling with in situ geochronology is noteworthy to unravel the protracted accretionary history within the Khammam region of the southeastern Indian shield.

In this study, we investigated various localities in and around the KSB, which comprise a wide variety of lithologies, including metapelites of the KSB and quartzofeldspathic gneiss of the EGMB (Fig. 1b). We present detailed petrological observations, pseudosection modeling, and U–Th–(total) Pb monazite ages to determine the metamorphic P – T – t history of these distinct lithodemic units. The specific issues addressed in this study include: (a) the relationship between tectonic fabrics and different metamorphic assemblages in the metapelites and quartzofeldspathic gneisses and (b) the possible timing of various deformation and metamorphic events. Further, we wanted to evaluate whether the KSB represents a possible extension of the Vinjamuru Domain that is located in the Nellore Schist Belt (Fig. S1b), as suggested by Sangam and Pavanaguru (2013). Finally, these new results from the Khammam region are combined with existing data to discuss its implications to counterparts in Columbia and Rodinia assemblages.

Geological background

The NNE–SSE trending Nellore–Khammam schist belt (NKSB) has traditionally been regarded as a collision orogenic belt that was sandwiched between the Archean EDC to the west and the Proterozoic EGMB to the east (Fig. S1; Leelanandam and Reddy 1988; Ramam and Murty 1997; Hari Prasad et al. 1999; Okudaira et al. 2001). The curvilinear NKSB extends for 600 km in length with variable width between 30 and 130 km (Fig. S1b; Okudaira et al. 2001). Based on lithological and geochronological data, the NKSB has been subdivided into the Nellore Schist Belt (NSB) and Khammam Schist Belt (KSB) in the south and north, respectively (Fig. S1b; Hari Prasad et al. 1999; Okudaira et al. 2001). The NSB comprises amphibolite facies Vinjamuru Domain and greenschist facies Udayagiri Domain (Fig. S1b). According to Sangam and Pavanaguru (2013), the upper amphibolite facies KSB rocks are considered the northern extension of the Vinjamuru Domain. The KSB lithologies form the basement to the Proterozoic-age Pakhal Group of rocks and Phanerozoic-age Gondwana sediments (Fig. 1b; Rajneesh Kumar et al. 1999). The eastern part of the KSB sporadically exposes parts of the Ongole Domain of the EGMB (Figs. 1b and S1b), typically dominated by high-grade enderbite and charnockite rocks (1.72–1.70 Ga; Kovach et al. 2001; Dobmeier and Raith 2003). Based on the existing geological

and isotopic data, the NKSB and Ongole Domain together constitute the Krishna Province (Figs. 1 and S1), represents a discrete crustal province in the southern part of the EGMB (Dobmeier and Raith 2003; Sharma 2009). The present study area in the Khammam region is situated along the northwestern boundary of the Krishna Province (Figs. 1a and S1).

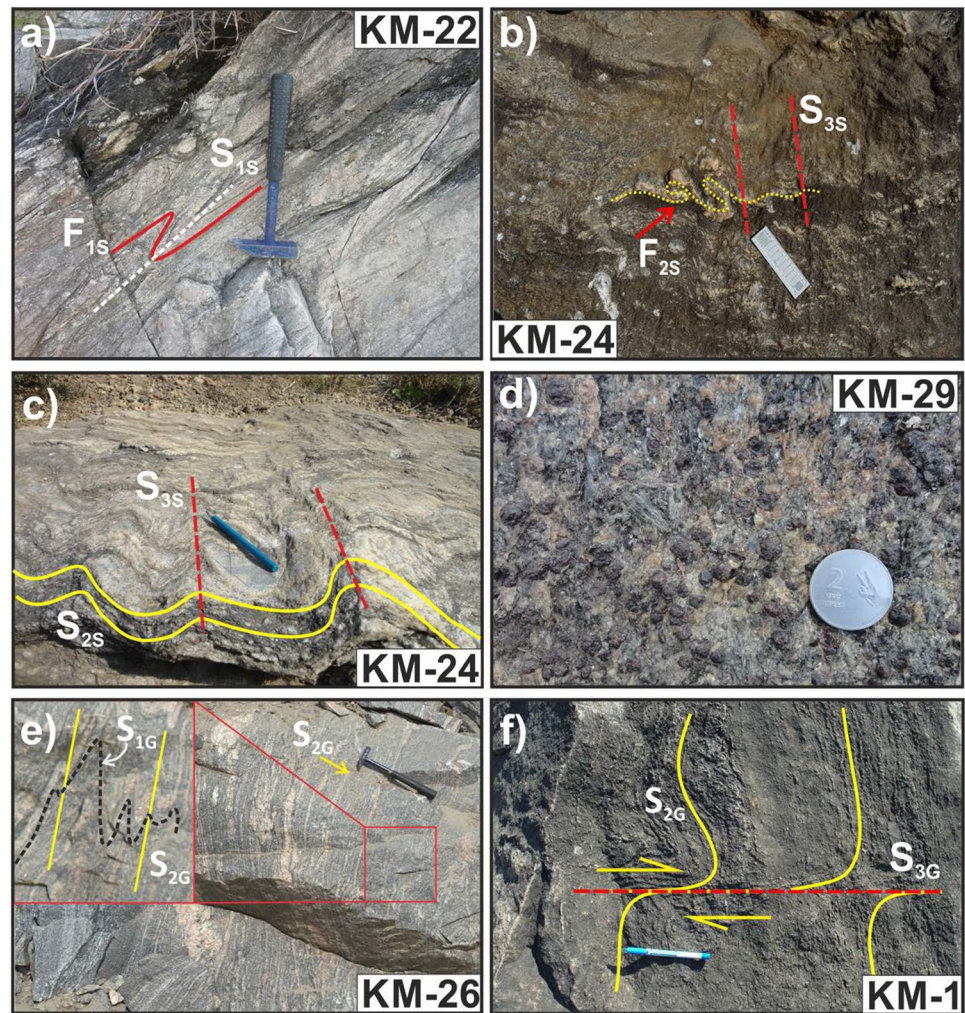
The KSB (Fig. 1b) comprises various lithological units, including metapelites, amphibolites, phyllites, and quartzites (Ramam and Murty 1997; Hari Prasad et al. 1999; Okudaira et al. 2001; Vijaya Kumar et al. 2006). The amphibolites are the most abundant lithology in the KSB and experienced three stages of deformation (D_1 , D_2 , and D_3 ; Hari Prasad et al. 1999). The F_1 and F_2 folds were formed by two-stage (NE–SW and NW–SE directional) compressional events, while F_3 folds were developed as a result of NW–SE shearing. In contrast, Rajneesh Kumar et al. (2000) identified four deformation events from the KSB lithologies. However, the metamorphic and geochronological evolution of the KSB is poorly investigated in previous studies. Hari Prasad et al. (2000) identified a high- T metamorphic event in the KSB amphibolites, which was dated using Sm–Nd mineral isochron at 824 ± 43 Ma (Okudaira et al. 2001). To determine the comprehensive geodynamic setting of this terrane, it is important to establish P – T – t constraints from all the involved lithologies during the accretion process. Hence, the lack of comprehensive information on metamorphic evolution and petrologically constrained age data from the KSB metapelites and associated lithologies allow us to revisit the KSB and its adjacent domains.

Field relations and structural setting

In this study, we focused on the Khammam region that is located in the western portion of the EGMB (Figs. 1b and S1b). The investigated lithologies include: (a) metapelites of the KSB, and (b) quartzofeldspathic gneisses of the EGMB (Figs. 1b, 2a–h). The sample locations are shown in Fig. 1b.

In the northeastern part of the Khammam region, metapelites of the KSB occur as discontinuous exposures within amphibolites of the KSB and migmatitic gneisses of the EDC (Fig. 1b). The contact relations between these lithologies are highly obscure, which might have shared a basement–cover relationship. The metapelites include garnet–biotite–muscovite \pm chlorite schists, garnet–kyanite schists, and phyllites (Fig. 2a–d). These metapelites have recorded three episodes of deformation (D_{1S} , D_{2S} , and D_{3S}), which resulted in the development of S_{1S} , S_{2S} , and S_{3S} tectonic fabrics (Figs. 1c and 2a–c). Tight isoclinal folds on primary foliation characterize the D_{1S} deformation in metapelites (Fig. 2a). The possible recumbent folding on early S_{0S}/S_{1S} foliation develops gently dipping S_{2S} axial

Fig. 2 Field photographs showing lithological and structural relations from **a–d** the KSB metapelites and **e–f** quartzofeldspathic gneisses and charnockites of the EGMB. Photographs **b**, **d**, and **f** are in plan view, and the remaining images represent section view. In the plan view, photographs, pencil, marker, and hammer-head point north direction. **a** Tight isoclinal folds on early S_{0S} foliation with the development of S_{1S} axial planar fabric in schistose rocks. **b** The image shows possible recumbent geometry of F_{2S} folds, which are interfolial to the S_{2S} foliation. **c** Plan view showing spaced S_{3S} crenulation cleavage on gently dipping S_{2S} schistosity. Note that the F_{3S} folds are plunging gently towards NNE. **d** The general appearance of garnet–kyanite schist within the supracrustal sequence. Note the presence of profuse garnet and kyanite porphyroblasts. **e** Banded foliation (S_{2G}) in quartzofeldspathic gneiss, defined by sub-parallel leucosomes. The inset shows vestiges of folded S_{1G} early foliation intrafolial to the S_{2G} planes. **f** Development of shear foliation (S_{3G}) in response to dextral shears within charnockites of the EGMB



planar fabric during the D_{2S} deformation (Fig. 2b). The NE–SW to NW–SE striking pervasive ($< 30^\circ$ dip) S_{2S} foliation is defined by the shape-preferred orientation of muscovite + biotite + kyanite mineral aggregates (Fig. 2d). However, the existence of recumbent geometry for F_{2S} folds is restricted to specific locations (Fig. 2b). During D_{3S} deformation, the S_{2S} schistosity is crenulated and produces NNE–SSW-trending steep S_{3S} axial planar fabric with gently plunging ($< 30^\circ$) F_{3S} folds towards NNE (Figs. 1c, 2c).

The exposures of EGMB quartzofeldspathic gneisses in the study area are typically restricted to the eastern portion of the Khammam region (Fig. 1b). The rock is represented by sub-centimeter to centimeter-scale quartzofeldspathic layers with variable proportions of garnet, biotite, quartz, plagioclase, and sillimanite (Fig. 2e). These gneisses were migmatized, and leucosomes were often folded (Fig. 2e). The steeply ($> 70^\circ$) dipping ENE–WSW-trending S_{2G} foliation defines the pervasive tectonic trend in the quartzofeldspathic gneiss of the EGMB (Figs. 1d, 2e). The remnants of early S_{1G} foliation are preserved intrafolial to the penetrative S_{2G} foliation in low-strain zones of the

D_{2G} deformation (inset in Fig. 2e). The leucosome layers are transposed along the S_{2G} foliation, suggesting that the possible partial melting in quartzofeldspathic gneisses was syntectonic to the D_{2G} deformation. Further, the S_{2G} foliations in associated charnockites are displaced by later dextral shears, producing N–S-trending and steeply dipping ($> 70^\circ$) S_{3G} foliation (Fig. 2f).

Methods

Electron probe microanalysis

Mineral compositions were determined using a CAMECA SX-FIVE electron probe microanalyzer (EPMA) equipped with five wavelength-dispersive spectrometers at the Department of Earth Sciences, Indian Institute of Technology Bombay (India). A focused beam with 15-kV accelerating voltage and 20-nA beam current was used during the silicate analyses. Calibration was performed using mineral standards including albite (Si,

Na), diopside (Mg), Al_2O_3 (Al), K-feldspar (K), Fe_2O_3 (Fe), rhodonite (Mn), Cr_2O_3 (Cr), TiO_2 (Ti), ZnS (Zn), BaSO_4 (Ba), apatite (Ca, F) and NaCl (Cl). Each analysis was performed for ~ 2 min, in which peak and background counts for all elements were measured for 20 s and 10 s, respectively. The X-PHI method was used for correcting matrix absorption effects (Merlet 1992). For identifying zoning patterns, X-ray element mapping of garnet was performed with operation conditions of 15-kV accelerating voltage, 50-nA beam current, and 50–70 ms dwell time per pixel. The detailed mineral compositions of various lithologies are presented in Table S1.

EPMA monazite dating was performed with a focused beam using 20-kV accelerating voltage and 200-nA beam current. ThM_a , UM_b , and PbM_a X-ray lines were calibrated using Th-glass, U-glass, and crocite standards. Simultaneously, two LPET crystals were employed in analyzing ThM_a (160 s), UM_b (160 s), and PbM_a (240 s) X-ray lines. The error propagated during monazite dating primarily depends on the precise estimation of ThO_2 , UO_2 , and PbO compositions, and uncertainties associated with the calibration of other elements and monazite standards (Jercinovic et al. 2012; Prabhakar 2013). Since these elements were analyzed for long counting times, the sub-counting method (5 cycles) was employed to minimize the effects of sample surface damage on the peak-background measurements of ThM_a , UM_b , and PbM_a (Spear et al. 2009). The measured intensity of PbM_a was corrected for the interference of $\text{ThM}_2\text{-O}_4$, $\text{ThM}\zeta_1$, $\text{ThM}\zeta_2$, YL_{C_2} , YL_{C_3} , and LaL_a intensities, whereas UM_b was corrected for ThM_c and $\text{ThM}_3\text{-N}_4$ interferences (Deshmukh et al. 2017). The resultant data were processed using the chi-square test to exclude inconsistent and anomalous counts and minimize error propagation on the final quantification of ThO_2 , UO_2 , and PbO concentrations (Prabhakar 2013). Further, empirical calibrations were typically associated with external uncertainties of 0.8%, which were propagated through the acquisition of ThO_2 , UO_2 , and PbO compositions (Dahl et al. 2005). Therefore, the counting errors obtained for monazite dates are additionally corrected for external uncertainties and are presented with 2σ errors (95% confidence level). The Steenkampskrall monazite standard (SHRIMP age: 1030 ± 6 Ma; Knoper et al. 2000) was used for monitoring the spectrometer and analytical drift during the monazite analysis.

High-resolution X-ray element maps were acquired to distinguish various compositional domains within the texturally constrained monazite grains. The methodology for identifying and retrieving meaningful populations from each compositional domain was adopted from Jercinovic and Williams (2005) and Williams et al. (2006). The monazite dates from each domain were

processed and presented graphically using the Isoplot program (version 4.15; Ludwig 2003). The detailed monazite compositions along with spot dates ($\pm 2\sigma$) are given in Table S2.

Bulk rock analysis

Bulk rock compositions of metapelites and quartzofeldspathic gneiss were estimated using inductively coupled plasma atomic emission spectrometry (ICP-AES) at the Department of Earth Sciences, IIT Bombay. A solution was prepared for 0.25 g of the sample by using the fusion method (Sheth et al. 2011), in which the matrix comprises 0.75-g lithium metaborate (LiBO_2) and 0.50 g of lithium tetraborate (LiB_4O_7). Geological Survey of Japan and United States Geological Survey reference materials (JG-2, JG-3, Jb-1b, and JGb-2) were used in the calibration, and rhyolite standard (JR-3) was reanalyzed at regular intervals to monitor the instrument drift. The whole-rock compositions of studied samples are given in Table S3.

Phase equilibria modeling

Pseudosection modeling was performed for the metapelite (KM-24 and KM-29) and quartzofeldspathic gneiss (KM-26C) samples from the Khammam region. The modeling was carried out in the NCKFMASHT system using the bulk composition obtained from ICP-AES analyses (Table S3). Fe_2O_3 was omitted in phase equilibria modeling due to the following reasons: (a) absence of Fe^{3+} rich phases (e.g., magnetite) in the equilibrium mineral assemblages, (b) Fe^{3+} content is negligible in key minerals, and (c) the occurrence of ilmenite in the equilibrium mineral assemblage implies low oxidation conditions (Diener and Powell 2010; Groppo et al. 2010). The consideration of MnO in the phase equilibria calculations shifts the garnet stability field towards lower-pressure conditions (e.g., Tinkham et al. 2001 and references therein). Besides, the effect of MnO on the stability (modal abundance) of other common minerals is negligible. Thus, a similar topology is observed in pseudosections with MnO as compared to those computed without MnO content (White et al. 2004). Therefore, the effect of MnO was ignored in the phase equilibria modeling of metapelites and quartzofeldspathic gneiss. The H_2O content was adjusted so that the equilibrium assemblage will be stabilized with appropriate water content (Table S3). The effect of H_2O on the modeling was determined by $T\text{-}M_{\text{H}_2\text{O}}$ diagrams (Figs. S4a–c and S5b, c, e). Pseudosections were constructed using the Perple_X software program (version 6.8.6; Connolly 2005) with the internally consistent thermodynamic data set file (hp62ver.dat) after Holland and Powell (1998), which was updated in 2011. The activity–composition ($a\text{-}x$) solution models used in this study are garnet, biotite, white mica,

cordierite, orthopyroxene and silicic melt (White et al. 2014), K-feldspar (Waldbaum and Thompson 1968), plagioclase (Newton et al. 1980), and spinel (White et al. 2002).

The P - T phase diagrams constructed using pseudosection modeling are typically associated with several notable errors, which limit our interpretation of results determined for complex mineral assemblages (Palin et al. 2016). The choice of bulk composition is one of the important factors in estimating the best quality results from the pseudosection modeling of a heterogeneous sample. Often, the precise estimation of bulk composition is challenging, and most times, it represents a poor analogue of composition in which the equilibrium mineral assemblages were stabilized (Connolly and Petrini 2002). Further, the uncertainties associated with the a - x relationships of end-member minerals were propagated through to the final P - T results, together with bulk-composition-related errors (Holland

and Powell 2011 and references therein). In view of the limitations mentioned earlier, bulk compositions acquired using ICP-AES analyses (in this study) were correlated with those calculated using mineral modes from thin sections. The difference between these results is negligible. Besides, appropriate solution models with updated thermodynamic data sets were considered during pseudosection computations.

Results

Sample description, petrography, and mineral compositions

In this section, we describe sample locations, metamorphic textures, and mineral assemblages (Figs. 1, 3, 4, 5) from garnet-bearing metapelites (KM-29 and KM-24) of the

Fig. 3 Detailed petrographic and microtextural relations from metapelites of the KSB. **a** Garnet porphyroblast in sample KM-29 consists of biotite, ilmenite, and rutile inclusions. Note that the matrix foliation (S_{2S}) defined by muscovite and quartz aggregates wraps around garnet porphyroblast. **b** Large kyanite grains are oriented along with the S_{2S} fabric and contain inclusions of biotite and muscovite. **c** Kyanite- and muscovite-defined foliation (S_{2S}) wrapping the garnet porphyroblast. Note the bending of kyanite grains (arrow) while wrapping around the garnet. **d** Two types of biotite grains are identified in the matrix foliation of metapelites. Bt_{II} defines the S_{2S} fabric, whereas Bt_{III} replaces muscovite and K-feldspar in the matrix. **e** Small garnet crystals ($\sim 500 \mu\text{m}$) associated with S_{2S} foliation, and **f** elongated kyanite crystals oriented parallel to the matrix foliation (S_{2S}) in sample KM-24

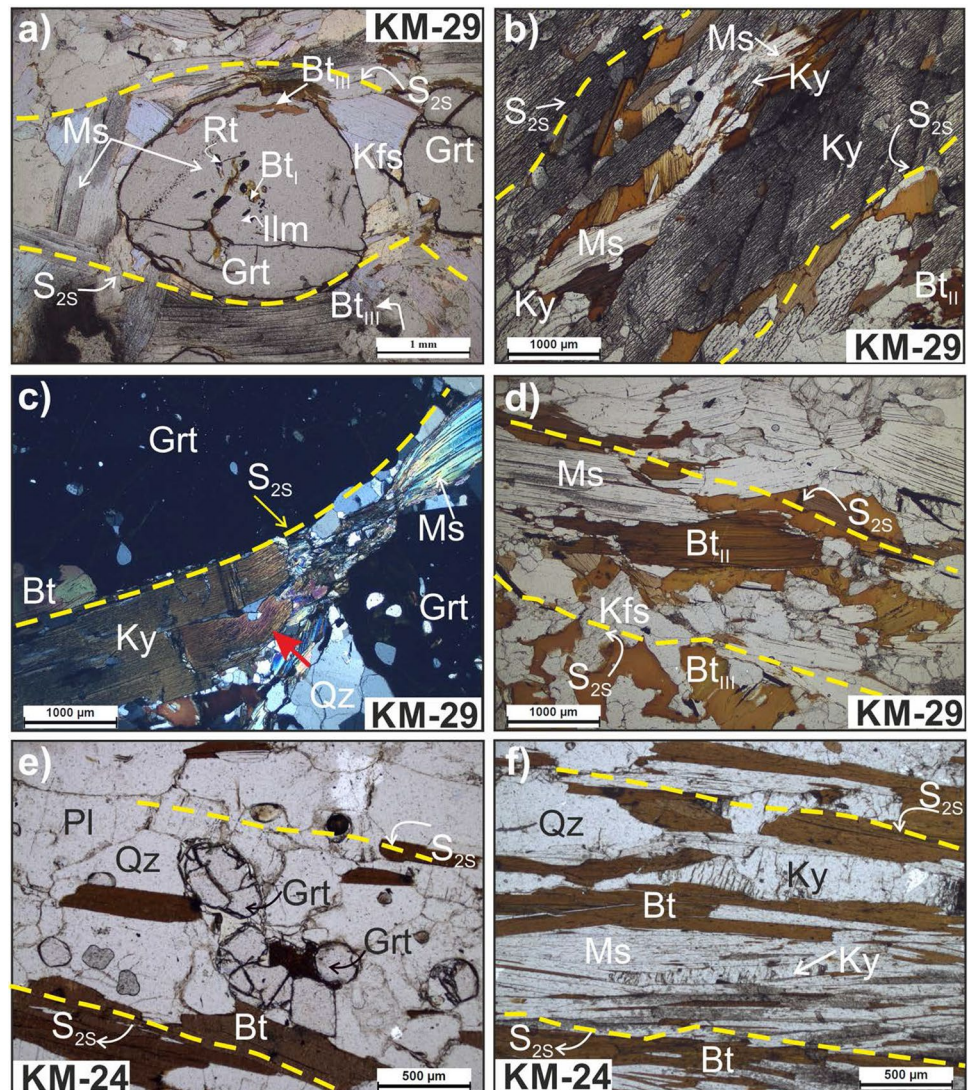
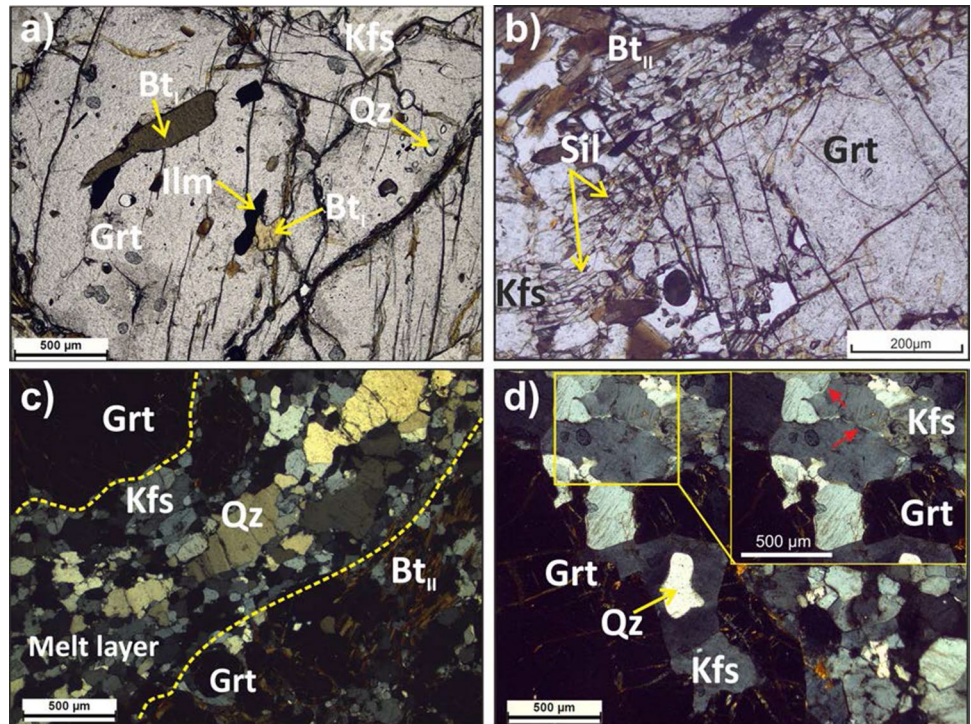


Fig. 4 Petrographic and microtextural relations from quartzofeldspathic gneiss (KM-26C) of the EGMB. **a** Garnet porphyroblast with inclusions (arrows) of an early assemblage consisting of ilmenite, biotite, and quartz. **b** Growth of sillimanite (arrows) and biotite along the grain boundaries of garnet porphyroblasts. **c** Large ribbon-shaped quartz aggregates within the K-feldspar matrix and quartz-defined leucosomes layer (dashed lines). **d** Thin films of optically continuous K-feldspar filling the grain boundaries (red arrows, enlarged view). Note the cusps to lobate K-feldspar enclosing anhedral quartz (yellow arrow), indicating partial melting in sample KM-26C



a	Mineral Phase	D _{1S} (?)		D _{2S}		D _{3S}		
		Early	Late	Early	Late	Early	Late	
		Prograde(M _{PR})		Peak(M _P)		Post-Peak(M _{PP})		
Garnet-Kyanite Schist (KM-29)	Garnet	—————					
	Kyanite	—————					
	Biotite	Bt _i (TiO ₂ = 4-5%)		Bt _i (TiO ₂ = 3-4%)		Bt _i (TiO ₂ = 1-2%)		
	Muscovite	—————					
	K-feldspar	—————					
	Rutile	—————					
	Ilmenite	—————					
	Quartz	—————					
Prograde (M _{PR}):		Grt+Ilm+Ms+Bt _i +Qz+Rt				Peak (M _P): Ky+Grt+Ilm		
Post-Peak (M _{PP}):		Ky+Grt+Ilm+Ms+Bt _i +Qz+Kfs				+Ms+Bt _i +Qz+Kfs		
b	Mineral Phase	D _{1G} (?)		D _{2G}		Post-D _{2G}		
		Prograde(M _{PR})	Peak(M _P)	Post-Peak(M _{PP})				
		Prograde(M _{PR}):		Peak(M _P):		Post-Peak(M _{PP}):		
Quartzofeldspathic Gneiss (KM-26C)	Garnet	—————			
	Sillimanite	—————			
	Biotite	Bt _i		Melting		Bt _i		
	K-feldspar		
	Ilmenite	—————			
	Quartz	—————			
Prograde (M _{PR}):		Grt+Bt _i +Ilm+Qz±Kfs		Peak(M _P):		Grt+Melt+Ilm+Qz+Kfs+Bt _i		
Post-Peak (M _{PP}):		Grt+Sil+Ilm+Bt _i +Qz+Kfs						

Fig. 5 Schematic diagram describing the growth of various minerals in relation to the deformation and metamorphic events from the samples **a** KM-29 and **b** KM-26C

KSB and quartzofeldspathic gneiss (KM-26C) of the EGMB. Mineral abbreviations used in this section are after Whitney and Evans (2010).

Sample KM-29

Sample KM-29 was collected from an isolated outcrop ~ 20 km southwest of the Kothagudem town (Fig. 1b). The sample contains garnet porphyroblasts within a matrix defined by biotite + kyanite + muscovite + K-feldspar + quartz + ilmenite (Fig. 3a–d). The garnet porphyroblasts (3–6 mm) occur commonly as subhedral grains with inclusions of biotite, muscovite, ilmenite, rutile, and quartz (Fig. 3a). Rutile is only observed as inclusions within the garnet porphyroblasts. The wrapping of muscovite-defined S_{2S} foliation around garnet suggests that these porphyroblasts were formed pre-tectonic to the D_{2S} deformation (Fig. 3a). Inclusion minerals are completely absent in the rim portion of the garnet (Fig. 3a). The garnet exhibits weak core–rim compositional zoning (Prp_{10–11}Alm_{85–88}Grs_{1.7–2.6}Sps_{2.1–2.6}) with an increase of grossular content towards the rim along with slight variations in pyrope, almandine, and spessartine contents (Table S1; Fig. S2a). These minor compositional variations from the core to the rim of garnet porphyroblast suggest long-lasting peak metamorphism at temperature conditions ≥ 600 °C, which significantly homogenizes prograde zoning patterns of the garnet core through intracrystalline diffusion (cf. Spear and Florence

1992; La Roche et al. 2015). This is also evident from the flattened compositional profile of garnet (Fig. S2a) in sample KM-29. The kyanite porphyroblasts usually consist of quartz, muscovite, and biotite inclusions (Fig. 3b), aligned parallel to the S_{2S} fabric, and show slight bending as it wraps the garnet porphyroblast (Fig. 3b, c). All these textures indicate that the growth of kyanite postdates the garnet and syntectonic with the D_{2S} deformation.

Biotite occurs as inclusions within garnet cores (Bt_I), and as large discrete grains (Bt_{II}) interleaved with matrix muscovite and quartz (Fig. 3a, b, d). Both these varieties of biotite crystals exhibit distinct composition. The inclusion-type biotite (Bt_I) grains are characterized by $X_{Fe}=0.58-0.59$, $TiO_2=4.0-5.0$ wt%, while the matrix biotite (Bt_{II}) grains contain slightly higher X_{Fe} (0.64–0.65) with lower TiO_2 (3.0–4.0 wt%) content (Fig. 3a, b, d; Fig. S3a; Table S1). Locally, fine-grained biotite aggregates replacing matrix minerals and garnet rims (Fig. 3a, d) are designated as retrogressive biotite (Bt_{III}). Biotite_{III} has X_{Fe} values ranging from 0.63 to 0.64 with TiO_2 content of 2.4–2.7 wt% (Fig. S3a; Table S1). Muscovite grains in the matrix are compositionally homogeneous with Na and Si contents variable between 0.06–0.08 apfu (atom per formula unit) and 3.00–3.10 apfu. K-feldspar grains in the matrix have a uniform composition with X_{or} value ranging from 0.84 to 0.89 (Table S1).

According to the aforementioned petrographic observations, inclusion-bearing garnet core along with inclusion minerals were stable during the early-stage prograde metamorphism, while the inclusion-poor garnet core and syn- D_{2S} kyanite were considered to be part of the peak metamorphic assemblage (Fig. 5a). The prograde (M_{PR}) and peak (M_P) metamorphic assemblages are interpreted to be garnet (inclusion-rich core) + biotite_I + muscovite + ilmenite + rutile + quartz and garnet (inclusion-poor core) + kyanite + biotite_{II} + muscovite + ilmenite + quartz + K-feldspar, respectively (Figs. 3a, 5a). The post-peak retrogressive event (M_{PP}) is characterized by the replacement of garnet, kyanite, and muscovite with biotite_{III} along their grain boundaries, and diffusive compositional adjustment (change in the grossular content) of garnet towards the rim (Fig. 3a, b, d, Fig. S2a).

Sample KM-24

Sample KM-24 was collected from a flat-lying exposure located ~20 km east of the Khammam town (Fig. 1b). This sample consists mainly of garnet, biotite, kyanite, muscovite, plagioclase, quartz, and ilmenite (Fig. 3e–f). The growth of fine-grained (< 1 mm), subhedral, and inclusion-free garnet porphyroblast within the matrix foliation dominated by biotite and quartz suggests that the garnet has grown syntectonic with the S_{2S} foliation (Fig. 3e). The garnet ($Prp_{8-11}Alm_{82-84}Grs_{3.5-3.9}Sp_{3.5-4.2}$) is enriched

in almandine content with a low concentration of pyrope, grossular, and spessartine and exhibits uniform composition throughout the grain. Kyanite is mostly oriented along the S_{2S} foliation (Fig. 3f), which advocates the syn- S_{2S} growth of kyanite crystals. Biotite in the matrix has a uniform composition with X_{Fe} of 0.61–0.64 and TiO_2 of 1.9–2.9 wt%. The Na content in the matrix muscovite (0.10–0.19 apfu) is slightly higher than muscovite from sample KM-29 (Fig. S3b), while plagioclase grains are sodic with X_{ab} of 0.80–0.84 (Table S1). Based on the textural relations, the sample comprises the peak metamorphic assemblage (M_P) of garnet + kyanite + biotite + muscovite + ilmenite + plagioclase + quartz (Fig. 3e–f).

Sample KM-26C

Sample KM-26C was collected from an isolated outcrop located in the easternmost part of the Khammam region (near Kallur village; Fig. 1b). This sample is characterized by subidioblastic garnet porphyroblasts within the matrix composed of K-feldspar, quartz, and biotite (Fig. 4a–d). The garnet porphyroblasts are chemically homogeneous ($Prp_{14-16}Alm_{80-81}Grs_{3.5-3.9}Sp_{0.5-0.8}$) and often contain inclusions of biotite, quartz, ilmenite, and K-feldspar (Fig. 4a). Biotite grains as inclusions (Bt_I) in garnet and those in the matrix (Bt_{II}) have a similar composition with X_{Fe} between 0.61 and 0.65. Matrix K-feldspar has higher X_{or} content (0.83–0.90) than K-feldspar composition ($X_{or}=0.71-0.80$) in the leucosome portion (Table S1). Sillimanite occurs as acicular crystals, associated with the garnet along its grain boundaries (Fig. 4b). The leucosomes (Fig. 2e), represent the migmatized portion of sample KM-26C, are characterized by K-feldspar and quartz minerals with cusped to lobate outlines (Fig. 4c, d).

Based on the above observations, the inclusion minerals along with the garnet (M_{PR} : garnet (inclusion-rich core) + biotite_I + ilmenite ± K-feldspar) constrain the early prograde event in the sample KM-26C (Fig. 5b). The partial melting in quartzofeldspathic gneiss (Fig. 4a, b) marks the peak metamorphism (M_P : garnet (inclusion-poor core) + K-feldspar + biotite_{II} + quartz + melt), which might have homogenized the prograde garnet composition due to high-grade metamorphism (Fig. S2c). The post-peak metamorphism (M_{PP}) is marked by sillimanite growth along the subhedral margins of garnet, and minor compositional readjustments in biotite_{II} and garnet rim compositions (Fig. 4b and Fig. S2c).

Conventional thermobarometry

The equilibrium P – T conditions of various metamorphic episodes in metapelites (KM-24 and KM-29) and quartzofeldspathic gneiss (KM-26C) were determined

Table 1 Summary of conventional thermobarometry results obtained for metapelites (KM-24 and 29) and quartzofeldspathic gneisses (KM-26C) in the Khammam region

Sample	Lat-Long	Mineral Pairs	Metamorphic stage	Thermometers (T in °C)					Barometers (P in kbar)			
				Grt–Bt		Ti-in-Bt			GBPQ	GBAQ	GASP	
Garnet-kyanite schist of KSB				1 (GS)	2 (HW)	3	4	5	6	7	8	9
KM-24	17° 12' 10" 80° 28' 21.9"	Grt(c)–Bt(m)/Ms(m)	M_p	613	612	620	639	630 ± 30	6.2	6.0	7.0	7.2
KM-29	17° 25' 8.4"	Grt(c)–Bt _{II} (m)/Ms(m)	M_p	623	627	617	657	695 ± 25	–	–	7.5	–
	80° 33' 41.4"	Grt(r)–Bt _{III} (n)	M_{pp}	566	568	613	561	650 ± 10	–	–	7.2	–
Quartzofeldspathic gneiss of EGMB				1 (GS)	2 (HW)	3	4	5	6	7	8	9
KM-26C	17° 16' 45"	Grt(c)–Bt _{II} (m)	M_p	722	721	720	836	715 ± 15	–	–	–	–
	80° 40' 45.1"	Grt(r)–Bt _{II} (n)	M_{pp}	729	726	716	820	–	–	–	6.9	–

(1) Battacharya et al. (1992); (2) Battacharya et al. (1992); (3) Holdaway (2000); (4) Ferry and Spear (1978); (5) Henry et al. (2005); (6) Hoisch (Fe) (1990); (7) Hoisch (Mg) (1990); (8) Wu (2017); (9) Holdaway (2001); GS–Ganguly and Saxena (1984); HW–Hackler and Wood (1989); other abbreviations: *c* core composition away from inclusions; *m* matrix biotite away from garnet; *n* nearest neighbor in contact with garnet; *r* outermost rim composition

using the application of mineral thermobarometry (Table 1). The temperature conditions were estimated using the garnet–biotite exchange thermometer (Ferry and Spear 1978; Bhattacharya et al. 1992; Holdaway 2000) and Ti-in-biotite thermometer (Henry et al. 2005). The pressure conditions were calculated using the garnet–biotite–plagioclase–quartz (GBPQ; Hoisch 1990), garnet–biotite–aluminum silicate–quartz (GBAQ; Wu 2017), and garnet–aluminum silicate–plagioclase–quartz (GASP; Holdaway 2001) barometers.

Based on the aforementioned textural relations, it is evident that the prograde garnet compositions (and inclusion minerals) in metapelites and quartzofeldspathic gneiss were homogenized due to intracrystalline diffusion induced during prolonged high-temperature peak metamorphism (cf. La Roche et al. 2015). Therefore, it is difficult to constrain the prograde metamorphic conditions using the compositions of garnet core and entrapped biotite inclusion. We have paired garnet core (distant from inclusions) and matrix biotite compositions, and garnet rim and biotite in contact with garnet compositions to determine the peak and post-peak P – T conditions, respectively. In sample KM-29, the mineral pairs represented by garnet core (inclusion-poor)–matrix biotite (Bt_{II}) and GBAQ assemblages recorded P – T conditions of 617–657 °C at 7.5 kbar (Table 1). These P – T conditions represent the peak metamorphic episode (M_p) for sample KM-29. The P – T conditions for post-peak metamorphism (M_{pp}) were retrieved using garnet rim–biotite (Bt_{III}) mineral pairs and GBAQ matrix mineral assemblages at 566–613 °C and 7.2 kbar. Similarly, the garnet and matrix minerals (biotite, kyanite, plagioclase, and quartz) yielded peak P – T conditions (M_p) of 612–639 °C at 6.0–7.2 kbar for sample KM-24 (Table 1). The calculations for garnet core (inclusion-poor)–matrix biotite (Bt_{II}) pairs in sample KM-26C yielded peak (M_p) temperature conditions of

720–836 °C. The peak pressure conditions could not be determined due to the lack of suitable mineral assemblages. The P – T estimates using garnet rim–biotite (Bt_{II}) in contact with garnet and GBAQ mineral assemblages yielded slightly lower temperature conditions of 716–820 °C at ~6.9 kbar (Table 1). These P – T values represent near-peak re-equilibrium conditions that stabilized sillimanite in the matrix assemblage.

P – T pseudosection modeling

Sample KM-29 (garnet–kyanite–K-feldspar schist)

The peak mineral assemblage (M_p) preserved in sample KM-29 comprises garnet core (inclusion-poor) + muscovite + biotite_{II} + K-feldspar + kyanite + quartz + ilmenite. In excess H₂O fluid conditions, the peak mineral assemblage is not stabilized in the P – T frame of NCKFMASHT pseudosection. To determine the actual H₂O content, a T – M_{H_2O} diagram was computed at 7.5 kbar, which is in the range of P – T estimates of conventional thermobarometry (7.2–7.5 kbar; Table 1). The H₂O content was considered between anhydrous ($M_{H_2O} = 0$) conditions and compositions with a maximum amount of H₂O ($M_{H_2O} = 1$) that is represented by the loss-on-ignition data (~7 mol%). In T – M_{H_2O} diagram, the peak assemblage is stable in the temperature conditions of ~480–720 °C at M_{H_2O} values of 0.10–0.65 (Fig. S5b). At $M_{H_2O} > 0.65$, kyanite is not stable in the predicted assemblage and stabilizes mineral assemblages with excess H₂O. Plagioclase is stable at lower temperatures (<480 °C), which is not a part of the peak mineral assemblage. To estimate appropriate M_{H_2O} content, a series of pseudosections were constructed at $M_{H_2O} = 0.27, 0.40, \text{ and } 0.60$ (Fig. S4a–c). Finally, we have considered the M_{H_2O} value of 0.55 (3.64 mol%; Fig. S5b) in the pseudosection modeling,

which gives the best approximation of calculated modal abundances of garnet (13–15 vol%), kyanite (2–3 vol%) and muscovite (22–24 vol%) as compared to observed values (Fig. S5a–b).

The P – T pseudosection for sample KM-29 was constructed in a P – T range of 4–9 kbar and 500–800 °C (Fig. 6a). The field-3 with garnet + muscovite + biotite + K-feldspar + kyanite + quartz + ilmenite marks the

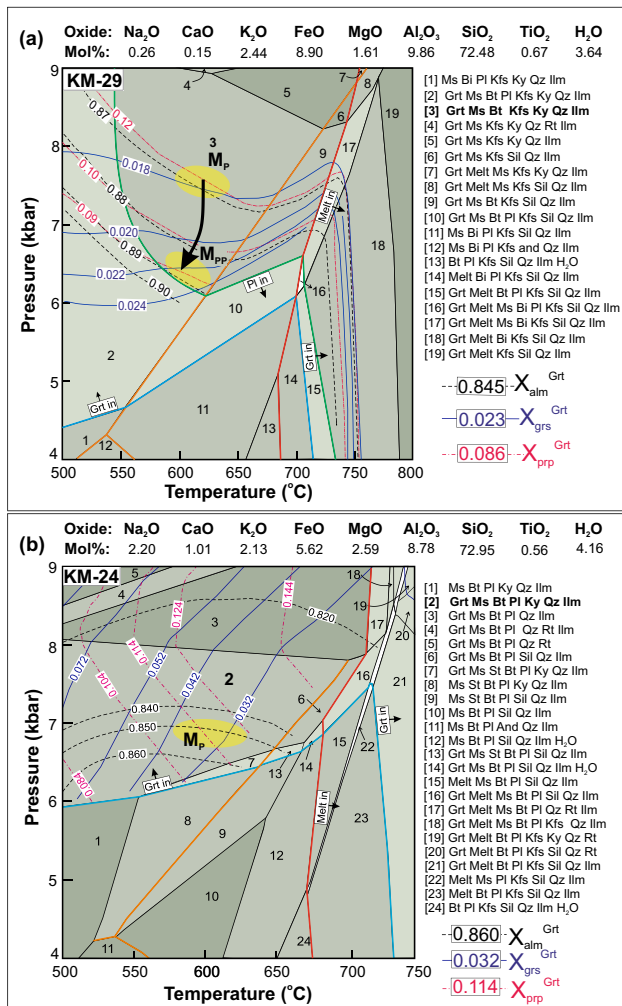


Fig. 6 Perple_X-generated phase diagrams constructed in the NCKF-MASHT system for samples **a** KM-29 and **b** KM-24. Bulk compositions (mol%) used in pseudosection calculations are given in the top parts of pseudosections. **a** A P – T pseudosection constructed for sample KM-29, modeled with compositional isopleths of garnet. The arrow indicates the inferred P – T trajectory from the core to the rim portion of the garnet (M_p to M_{pp}). **b** The modeled P – T pseudosection for KM-24 contoured with the garnet compositional isopleths. The thick red line in both pseudosections marks the solidus, while the green (in **a**) and blue (in **a** and **b**) thick lines demarcate the limits of plagioclase and garnet-bearing assemblages, respectively. The thick orange lines indicate the stability fields of andalusite, kyanite, and sillimanite. Yellow shades represent mineral isopleth intersections for the peak (M_p) and post-peak (M_{pp}) metamorphic assemblages

observed peak metamorphic assemblage (M_p), which stabilizes in a wide P – T window (6.0 to >9.0 kbar and 500–700 °C; Fig. 6a). The intersection of X_{alm} (Fe/[Fe + Mg + Ca]) = 0.87, X_{prp} (Mg/[Fe + Mg + Ca]) = 0.12 and X_{grs} (Ca/[Fe + Mg + Ca]) = 0.018 isopleths of garnet, which represent inclusion-poor garnet core composition, constrains the peak (M_p) metamorphic conditions at 7.4–7.8 kbar and 600–640 °C. The intersection of garnet rim isopleths ($X_{alm} = 0.89$, $X_{prp} = 0.10$ and $X_{grs} = 0.024$) retrieves P – T conditions for the post-peak adjustments (M_{pp}) at 6.1–6.6 kbar and 590–625 °C (Fig. 6a). These P – T estimates are in good agreement with the peak (617–657 °C at 7.5 kbar) and post-peak (566–613 °C and 6.0–7.2 kbar) metamorphic conditions calculated using the application of conventional thermobarometry (Table 1). On combining the P – T conditions of peak (M_p) and post-peak (M_{pp}) metamorphic episodes, a small decompression path ($\Delta P \sim 1.4$ kbar; calculated from average values) can be observed for the sample KM-29 (Fig. 6a). Although the pressure difference in this P – T path is closer to the typical uncertainty on pressure estimates (i.e., 1 kbar) in pseudosection calculations, it should be noted that the grossular content increases (1.8–2.4 mol%) towards the garnet rim. By considering these factors, the decompression path (M_p – $M_{pp} = \sim 1.3$ kbar; Fig. 6a) constrained for sample KM-29 appears to be valid and formed as a result of post-peak adjustments of garnet in response to decompression.

Sample KM-24 (garnet–kyanite–plagioclase schist)

A T – M_{H_2O} diagram was constructed at 7.0 kbar to determine the appropriate H_2O content for the pseudosection modeling of sample KM-24. In T – M_{H_2O} diagram, the peak assemblage (garnet + kyanite + plagioclase + muscovite + biotite + quartz + ilmenite) is stable at <670 °C with M_{H_2O} values between 0.75–0.85 (Fig. S5c). At $M_{H_2O} > 0.85$, kyanite is not stable in the predicted assemblage, and equilibrate mineral assemblages with excess H_2O . K-feldspar is stable at lower M_{H_2O} values (<0.65), which is not a part of the peak mineral assemblage. Based on these constraints, we have considered an average M_{H_2O} value of 0.80 (4.16 mol%; Fig. S5c) for the pseudosection modeling of sample KM-24. The pseudosection constructed for sample KM-24 shows the stabilization of peak mineral assemblage (M_p : garnet + kyanite + plagioclase + muscovite + biotite + quartz + ilmenite) for a wide range of P – T conditions at 5.0–7.8 kbar and 500–670 °C (field 2; Fig. 6b). The garnet porphyroblasts are compositionally homogeneous and not diagnostic in estimating the prograde evolution (Fig. S2b). The intersection of $X_{alm} = 0.85$, $X_{prp} = 0.11$ and $X_{grs} = 0.32$ isopleths of unzoned garnet constrain the P – T conditions of peak

metamorphism (M_p) at 6.6–6.8 kbar and 580–610 °C (Fig. 6b). The estimated peak metamorphic conditions are consistent with the results of conventional thermobarometry (612–639 °C at 6.0–7.0 kbar; Table 1), and also similar to those constrained for the sample KM-29 (Fig. 6a).

Sample KM-26C (quartzofeldspathic gneiss)

The observed peak metamorphic assemblage (M_p : garnet core (inclusion-poor) + K-feldspar + quartz + ilmenite + biotite_{II} + melt) is stable over a wide range of H_2O (Fig. S5e). At 7 kbar, which represents the minimum pressure estimated using the conventional thermobarometry approach, the peak assemblage is stable over a temperature range of 750–910 °C with an M_{H_2O} value of >0.15 (Fig. S5e). An M_{H_2O} value of 0.69 (2.55 mol%) is considered as appropriate water content to stabilize the peak assemblage (Fig. S5e). At this M_{H_2O} value (0.69), the observed modal abundances of garnet (20–23 vol%) and K-feldspar (40–45 vol%) are comparable with the measured mineral modes (Fig. S5d–e).

Since the sample KM-26C is migmatized, the bulk composition obtained using ICP-AES analysis represents the residual bulk composition after melt migration (or loss). This residual composition can only constrain the peak and post-peak conditions of the rock (Korhonen et al. 2013). The P – T pseudosection for the sample KM-26C (gneiss) was modeled in a P – T range of 4–10 kbar and 600–1000 °C using the residual bulk composition (Fig. 7a). The peak mineral assemblage (field 14) is stable at variable pressures and 750–850 °C (Fig. 7a). The intersection of garnet isopleths (X_{alm} vol% = 0.803, X_{prp} = 0.160, and X_{grs} = 0.039) yielded the peak metamorphic conditions at 790–810 °C and 7.9–8.1 kbar (Fig. 7a). The sillimanite-bearing post-peak assemblage is represented by the field with garnet + K-feldspar + sillimanite + quartz + ilmenite + biotite (field 7) assemblage, which is stable at P – T conditions of ~7 kbar and 740–750 °C (Fig. 7a).

The prograde evolution of a migmatized rock can be determined by recalculating the plausible protolith composition, which involves reintegrating melt lost from the system with the residual bulk composition (White et al. 2004; Diener et al. 2008). The experimental evidence of Rosenberg and Handy (2005) suggests that melt migration starts when the partial melting exceeds 7 vol% and some amount of melt may be retained in the grain boundaries, which can be approximated to ~1 vol% (Sawyer, 2001), resulting in the net loss of 6 vol% from the system in a single prograde melting event. For sample KM-26C, the down temperature melt reintegration procedure (Korhonen et al. 2013) was applied to reconstruct plausible protolith bulk composition. The first stage melt reintegration (by adding ~6 vol%, melt) was performed in the field of

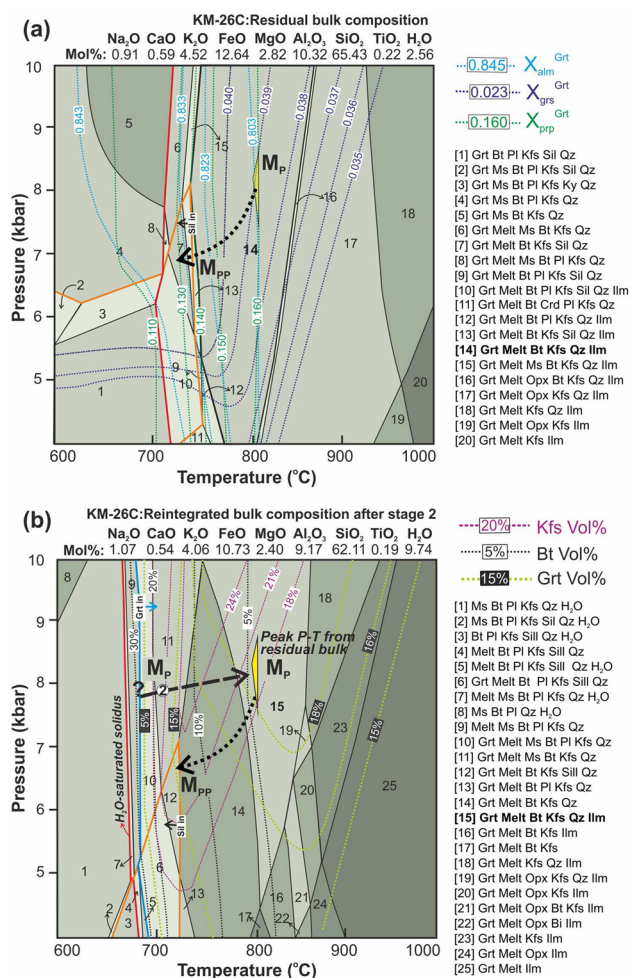


Fig. 7 **a** The P – T pseudosection for KM-26C was computed using the residual bulk composition, and the intersection of garnet isopleths constrains the peak metamorphic conditions (M_p ; yellow triangle). The post-peak P – T path is drawn to the sillimanite-bearing field (indicated by dotted arrow M_p – M_{pp}). **b** The pseudosection was derived after two-stage melt reintegration (12 vol%) procedure (see text; Fig. S6). The pseudosection is contoured with vol% of garnet, K-feldspar, and biotite to show the temperature dependency on their mineral modes. The thick red line in the pseudosection represents the solidus curve. The thick blue in **b** and orange line (**a** and **b**) demarcates the stability of garnet and sillimanite-bearing assemblages, respectively

peak assemblage garnet + K-feldspar + quartz + ilmenite + biotite + melt (field 14; Fig. 7a) at 800 °C and 8.0 kbar and the new bulk composition obtained after reintegration was used to compute a new pseudosection (Fig. S6a). Similarly, two-stage melt reintegration steps were performed by adding a total of 12 vol% of melt to the system to obtain the plausible protolith bulk composition with H_2O -saturated solidus (Figs. 7b and S6b). The pseudosection computed after reintegrating the melt with 12 vol% stabilized H_2O -saturated solidus at 660–680 °C with the plausible prograde assemblage of garnet + K-feldspar + quartz + ilmenite + biotite ± muscovite ± plagi-

class (Fig. 7b). Although muscovite and plagioclase are not observed in the sample, these minerals might have consumed on account of prograde heating and onset of the melting process (Fig. S6c).

The contoured modal isopleths of garnet, K-feldspar, and biotite in the pseudosection are steep and temperature dependent (Fig. 7b). Petrographic observations suggest that prograde garnet growth in the leucosome was contemporaneous with the partial melting and the consumption of inclusion phases like K-feldspar, biotite (\pm muscovite), and ilmenite (Figs. 4a and S6c). Therefore, a near-isobaric prograde P - T path ($M_{PR}-M_P$; $\sim \Delta T$ 100 °C) is inferred from the field of plausible prograde assemblage (field 10) to the peak P - T conditions (field 15) by considering the modal variations of garnet, K-feldspar and biotite (Figs. 7b). However, the prograde arm of this P - T path is not fully reliable due to the high uncertainty associated with pressure estimates of the prograde assemblage. The P - T estimates from peak to post-peak assemblage (M_P-M_{PP}) define a decompression path, which was consistent with the growth of fine-grained sillimanite and biotite in the matrix adjacent to garnet porphyroblast (Figs. 4b, 7a). These estimates infer a possible clockwise P - T path for the quartzofeldspathic gneiss, which involves a prograde melting (represented by dashed lines) event, followed by a decompression event on account of melt crystallization (Fig. 7a, b).

Monazite geochronology

In situ U-Th-(total) Pb monazite dating was performed on two samples, including a metapelite (KM-29) from the KSB and a quartzofeldspathic gneiss (KM-26C) from the EGMB. X-ray element maps (Th, U, and Pb) were combined with BSE images of monazites to identify discrete compositional domains (CD) (cf. Jercinovic and Williams 2005; Williams et al. 2006). These compositional domains are labeled as CD_S-I, II, and III for sample KM-29 and CD_G-I, II, III, IIIA, IV, and V for sample KM-26C (Figs. 8 and 9). The textural setting and compositional variation of analyzed monazite grains in these samples are summarized in Figs. 8, 9, and S7. The ThO₂ vs. Age, [Sm₂O₃ + Gd₂O₃] vs. [ThO₂], and Th/U vs. Age plots for various compositional domains in samples KM-29 and KM-26C are shown in Fig. S8.

KSB metapelite (KM-29)

Monazite in sample KM-29 mostly occurs in association with the matrix minerals, aligns parallel to the S_{2S} and S_{3S} matrix foliations, and is rarely observed as an inclusion within the garnet porphyroblasts (Figs. 8a-e and S7a-e).

The matrix monazite is generally grown as elongated grains (Figs. 8b-e and S7a), whereas inclusion-type monazite is anhedral to subhedral shape with sub-rounded edges (Figs. 8a and S7b-c). Th and Y monazite zoning patterns reveal three distinct compositional domains, CD_S-I, II, and III. The CD_S-I is represented by high-Th and low-Y (ThO₂ = 7–11%, UO₂ = 0.0–0.4%, Y₂O₃ = 0.8–1.2%) monazite cores (Fig. 8a), which are overgrown by relatively low-Th and comparable-Y CD_S-II (ThO₂ = 4–7%, UO₂ = 0.2–0.9%, Y₂O₃ = 1.0–1.1%), and low-Th and high-Y CD_S-III (ThO₂ = 5–6%, UO₂ = 0.9–1.9%, Y₂O₃ = 0.3–3.1%) domains (Fig. 8a-c). The integration of spot ages from chemically distinct CD_S-I and CD_S-II domains have yielded weighted mean ages of 1215 ± 13 Ma (MSWD = 0.85; n = 11) and 1137 ± 18 Ma (MSWD = 1.0; n = 7), respectively (Fig. 8f). Analyses from the monazite outer rims (CD_S-III) yielded a weighted mean age of 849 ± 06 Ma (MSWD = 1.3; n = 39).

EGMB quartzofeldspathic gneiss (KM-26C)

The subhedral to anhedral monazite grains from sample KM-26C are commonly hosted within garnet porphyroblasts, and K-feldspar, plagioclase, and quartz within the matrix (Fig. 9a-d). X-ray elemental maps of monazite grains can distinguish five discrete compositional domains, CD_G-I, II, III, IIIA, IV, and V in sample KM-26C (Fig. 9a-d). The CD_G-I domain is commonly preserved in the core of monazite-1 and is characterized by low-Th, -U, and -Pb domain (ThO₂ = 4–6%, UO₂ = 0.10–0.19%, PbO = 0.57–0.81%; Fig. 9a). This domain is overgrown by relatively high-Th, -U and -Pb domain (CD_G-II: ThO₂ = 8–13%, UO₂ = 0.25–0.50%, PbO = 1.0–1.7%). The monazite spot ages from CD_G-I yielded the oldest ages with a weighted mean age of 2689 ± 35 Ma (MSWD = 1.3; n = 11). The CD_G-II domain yielded a weighted mean age of 2494 ± 14 Ma (MSWD = 1.1; n = 24) (Fig. 9e). The CD_G-III with relatively high-Th and -U, and low-Pb (ThO₂ = 7–11%, UO₂ = 0.01–0.37%, PbO = 0.55–0.85%) is observed in the core portion of Mnz-3 (Fig. 9c). The CD_G-IIIA domain is characterized by relatively low-Th, U and Pb domain (ThO₂ = 4–6%, UO₂ = 0.01–0.40%, PbO = 0.3–0.5%, Y₂O₃ = 0.0–0.4%) preserved in the Mnz-2, Mnz-4 and also as outer rim overgrowing CD_G-II in Mnz-1 (Fig. 9a, b, d). Despite the variation in chemical compositions, the CD_G-III and CD_G-IIIA domains have shown a considerable overlap in their ages with weighted mean ages of 1621 ± 14 Ma (MSWD = 0.87; n = 13) and 1581 ± 15 Ma (MSWD = 0.79; n = 21), respectively (Fig. 9e). Further, these domains are overgrown by CD_G-IV (ThO₂ = 1–3%, UO₂ = 0.1–0.5%, PbO = 0.20–0.28%, Y₂O₃ = 0.0–0.2%) and CD_G-V (ThO₂ = 2–6%, UO₂ = 0.15–0.30%, PbO = 0.10–0.23%,

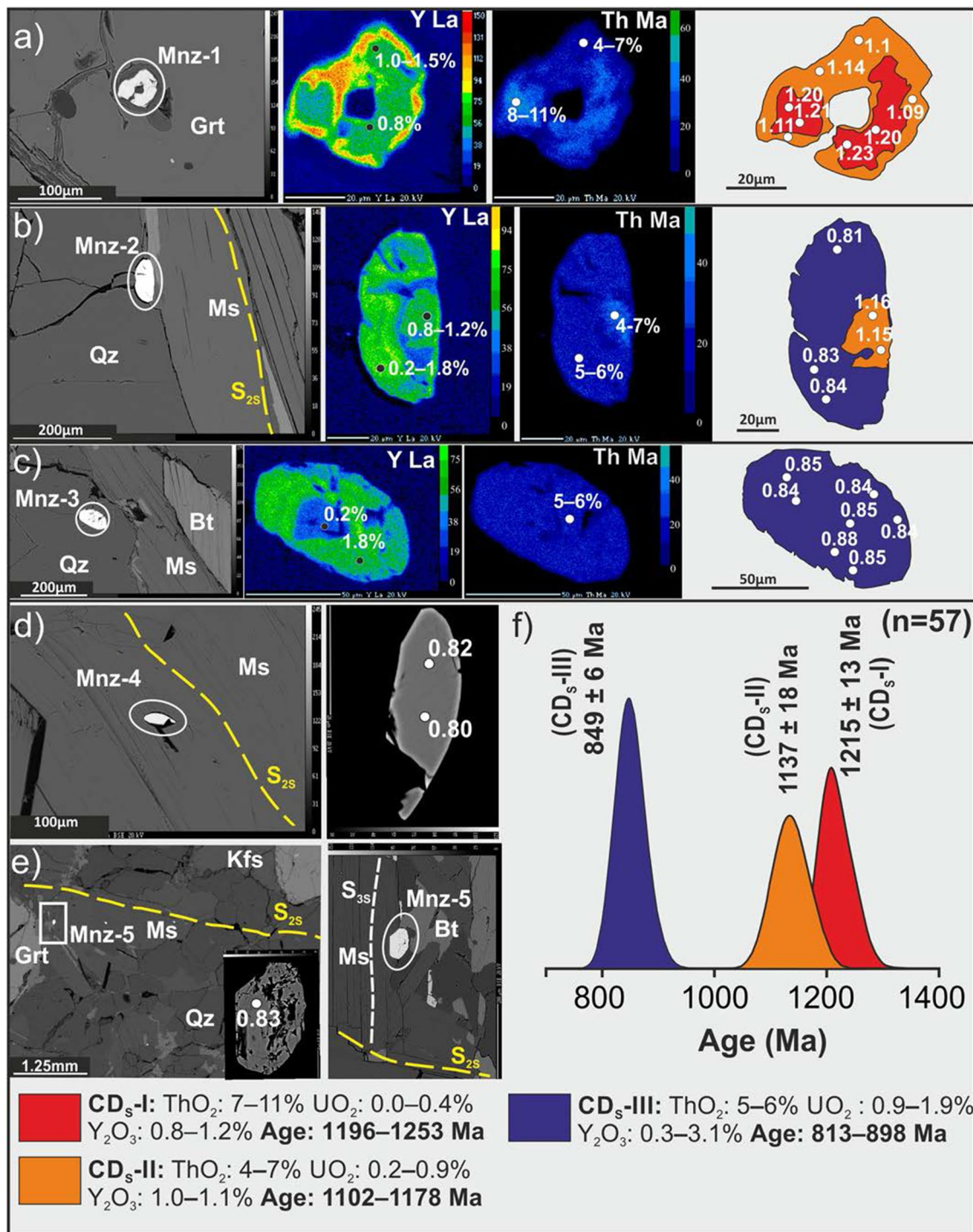


Fig. 8 a–e Textural occurrence and compositional variation of monazite grains in the metapelite (KM-29) of the KSB. **f** Probability density plot of monazite age data showing three distinct peak

ages (1215 ± 13 Ma, 1137 ± 18 Ma, and 849 ± 06 Ma) for various compositional domains (CD_S-I, CD_S-II, and CD_S-III) identified in the monazite grains. The spot ages given in the right panel are in ‘Ga’

Y₂O₃ = 0.0–0.2%) compositional domains (Fig. 9c). The CD_G-V is mostly preserved as thin rims over pre-existing chemical domains (Fig. 9b) and demarcates the final-stage monazite growth in the gneisses. Spot analyses provide

weighted mean ages of 1438 ± 25 (MSWD = 0.73; $n = 11$) and 869 ± 17 Ma (MSWD = 1.15; $n = 09$) for the CD_G-IV and CD_G-V domains, respectively (Fig. 9e).

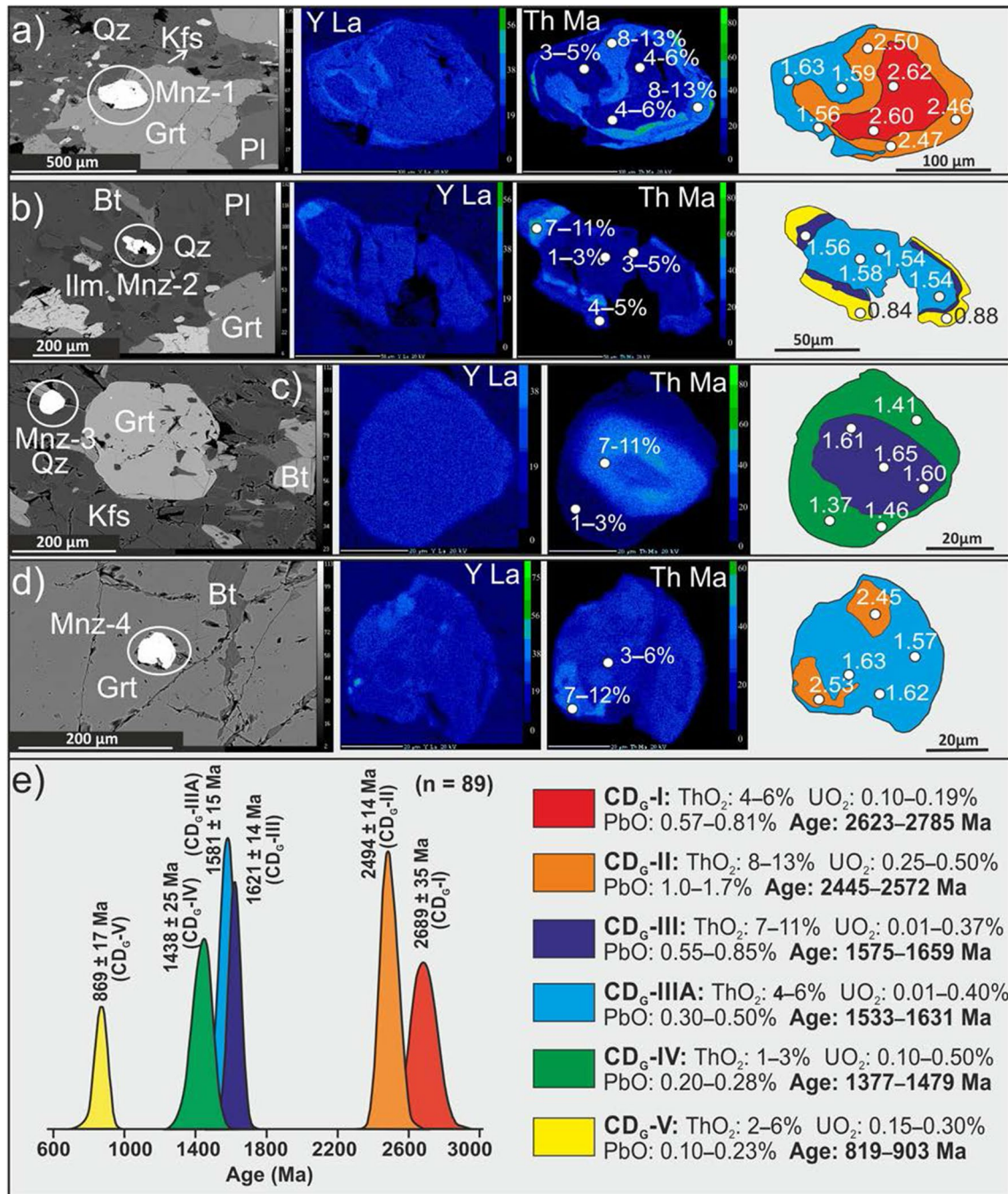


Fig. 9 a–d Textural occurrence and compositional variation of monazite grains in the quartzofeldspathic gneiss (KM-26C) of the EGMB. Note that these monazites are identified with five distinct compositional domains. e Probability density distribution of monazite age data show-

ing five different age peaks (2689 ± 35 Ma, 2494 ± 14 Ma, 1621 ± 14 Ma, 1581 ± 15 Ma; 1438 ± 25 Ma and 869 ± 17 Ma) from corresponding compositional domains (CD_G-I; CD_G-II; CD_G-III; CD_G-IIIa, CD_G-IV, and CD_G-V). The spot ages given in the right panel are in ‘Ga’

Discussion

Metamorphic P–T history and interpretation of monazite ages

The P–T histories and monazite age data described from the KSB metapelites and EGMB quartzofeldspathic gneisses are

hitherto unreported from the Khammam region (Figs. 1 and S1), barring those documented by Hari Prasad et al. (2000). The results acquired from petrological observations indicate that the KSB metapelites have recorded three stages (M_{PR}, M_P, and M_{PP}) of metamorphism. The garnet zoning patterns suggest that the inner core was completely homogenized due to the long-lived peak metamorphism (Fig. S2a, b).

Therefore, the inner core compositions are not reliable for estimating the prograde P – T conditions (La Roche et al. 2015). The prograde metamorphic stage probably initiated outside the P – T field of garnet and continued to stable after crossing the ‘garnet-in’ curve. Based on the wrapping S_{25} foliation around garnet, the prograde metamorphism (M_{PR}) should have occurred inter-tectonic between D_{15} and D_{25} deformation events. The peak metamorphism (M_P), accompanied by syn- D_{25} garnet (inclusion-poor core) and kyanite growth, is equilibrated at the P – T conditions of 7.4–7.8 kbar and 600–640 °C (Fig. 6a). The subsequent post-peak metamorphism (M_{PP}) at 6.1–6.6 kbar and 590–625 °C resulted in the diffusional adjustments of garnet rim and growth of biotite_{III} (Fig. 6a). The slight fall of pressure and temperature conditions from M_P to M_{PP} suggests a decompression path, which could have caused the exhumation of metapelites from ~ 26 km to ~ 22 km depth (Fig. 10c). The application of the melt reintegration procedure for quartzofeldspathic gneiss KM-26C constrains a near-isobaric prograde path (~ ΔT 100 °C; M_{PR} – M_P ; Figs. 7b and S6a, b). The subsequent partial melting, which resulted in the high-grade peak metamorphism (M_P) at

7.9–8.1 kbar/790–810 °C (Fig. 7a), is contemporaneous with the D_{2G} deformation (Fig. 2e). We assume that the increase of temperature from M_{PR} to M_P was caused by magmatic underplating, which occurred during the formation of the Ongole Domain of the EGMB (Sarkar and Schenk 2014; Sarkar et al. 2015). The formation of fine-grained sillimanite and biotite, around garnet (Fig. 4b), could be due to the post-peak readjustments (M_{PP}) at ~ 7 kbar/740–750 °C (Fig. 7a).

In metapelites, the Y budget of the monazite is mainly governed by the crystallization of garnet during sub-solidus metamorphism (Spear and Pyle 2010). Therefore, in the absence of other Y-bearing phases like xenotime, the Y partitioning between garnet and monazite can be used as a proxy to understand the relative timing of garnet growth and resorption (Mahan et al. 2006; Dumond et al. 2015; Rahimi and Massonne 2018). Monazites in KSB metapelites exhibit distinct chemical domains that have grown during different stages of metamorphism and deformation (Figs. 8 and S7). U–Th–(total) Pb dating of monazite cores with low-Y contents yielded two distinct age populations at 1253–1196 Ma (CD_{S-I}) and 1178–1102 Ma (CD_{S-II}) (Fig. 8a, b). The relatively older CD_{S-I} is exclusively seen

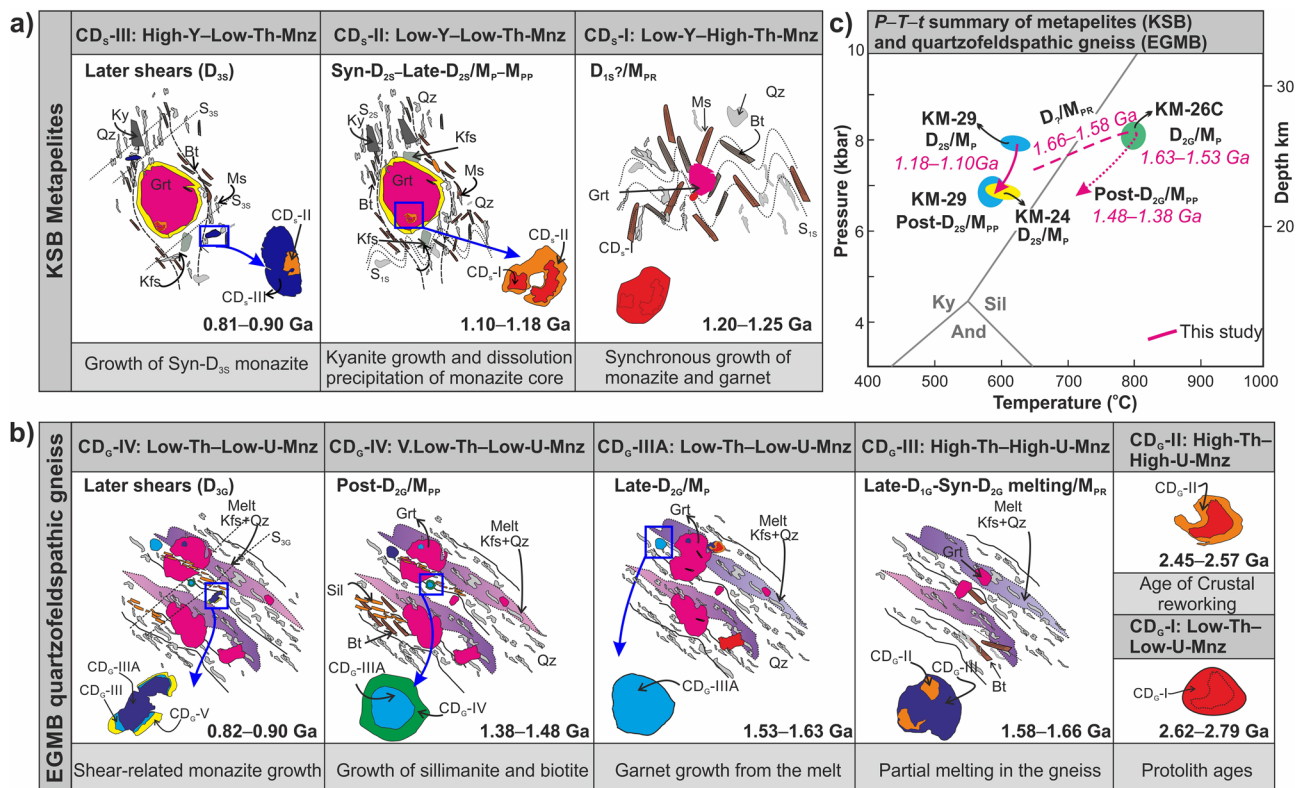


Fig. 10 Schematic diagram summarizes the various tectonothermal episodes and corresponding monazite ages identified in the **a** metapelite (KM-29) and **b** quartzofeldspathic gneiss (KM-26C). The top panels of these figures characterize compositional variation within different monazite age domains, while the bottom panels highlight

tectonic inferences suggested for each age population. **c** A P – T diagram summarizes various tectonothermal episodes and corresponding monazite ages for the samples KM-24, 29, and KM-26C in the Khammam region

as inclusion within the pre-D_{2S} garnet, whereas (Figs. 8a, and S7b, c) CD_S-II is noted as monazite overgrowth around CD_S-I, occupying core region in the matrix, and as discrete grains aligned parallel to the S_{2S} foliation (Figs. 8a, b, and S7d). In sample KM-29, xenotime is not stable in the equilibrium mineral assemblage, and therefore, Y preferentially partitions into garnet than monazite. Hence, the growth of the Y-poor core and rim (CD_S-I and II) of monazite could have formed simultaneously during the development of garnet porphyroblast. Based on petrographic textures (Figs. 3a and S7a), it is evident that the garnet growth initiated pre-tectonic to S_{2S} foliation. The above observations constrain the minimum timing for the prograde metamorphism (M_{PR}) at 1215 ± 13 Ma, where garnet growth was initiated during late-D_{1S} to early-D_{2S} deformation (Figs. 5a and 10a). The timing of peak metamorphism (M_P) is constrained at 1137 ± 18 Ma (Fig. 10a), which was consistent with the growth of CD_S-II monazite age domain and syn-D_{2S} kyanite (Fig. S7d). The much younger age at 849 ± 6 Ma, obtained from high-Y monazite rims (CD_S-III) and discrete matrix monazite grains overgrowing and crosscutting the S_{2S} foliation, at places aligned parallel to the S_{3S} foliation, represents the possible timing of the D_{3S} deformation (Figs. 8d, e, 10a, and S7e).

In quartzofeldspathic gneiss (KM-26C) of the EGMB, monazites hosted in the garnet show two distinct resorbed domains, CD_G-I and CD_G-II, which yielded weighted mean ages of 2689 ± 35 Ma and 2494 ± 14 Ma, respectively (Fig. 9a, d). These Neoproterozoic ages perhaps demonstrate the two separate reworking events that affected the pre-existing Archean crust (> 2700 Ma). The overgrowth of high-Th and low-Y domains (CD_G-III) with relatively high Th/U ratio (48–220) on highly resorbed monazite cores (CD_G-II) indicates the relative timing of partial melting in the gneiss. Since the Th and U preferentially fractionate into the melt, the monazite growing from this melt preferentially incorporates Th into its crystal structure (Xing et al. 2013), while U is retained in the melt (Keppler and Wyllie 1990), which is consistent with high Th/U ratio in domain CD_G-III (Fig. S8c). This CD_G-III domain is also characterized by relatively low-Sm and Gd ($\text{Sm}_2\text{O}_3 = 1.2\text{--}2.0\%$ and $\text{Gd}_2\text{O}_3 = 0.3\text{--}0.50\%$) compared to younger compositional domains (CD_G-IV and CD_G-V; Fig. S8d). This low-Sm and Gd is attributed to the growth of garnet that preferentially sequesters these elements during high-grade metamorphism (cf. Bea and Montero 1999). The CD_G-III compositional domains consistently yield ages between 1659–1575 Ma and characterize the timing of the partial melting and garnet growth. Thus, the timing of initial partial melting and garnet growth can be constrained at 1621 ± 14 Ma (MSWD = 0.87; $n = 13$). The relatively younger ages of 1631–1533 Ma (weighted average: 1581 ± 15 Ma; MSWD = 0.79; $n = 21$) were acquired from Th- and U-depleted domains (CD_G-IIIA), usually seen as overgrowing CD_G-II and as

independent grains within the matrix (Fig. 9a, b, d). This domain is characterized by a relatively high concentration of Sm and Gd (Fig. S8d), suggesting its growth from relatively Th-poor residual melt after forming the CD_G-III domain. At this stage, garnet growth might have ceased, and the monazite formed from residual melt enriched in Sm and Gd ($\text{Sm}_2\text{O}_3 = 2\text{--}3\%$ and $\text{Gd}_2\text{O}_3 = 0.50\text{--}1.54\%$) as compared to CD_G-III domain (Figs. 10b and S8d). Based on the monazite compositional variation and garnet growth, we interpret that transition from the prograde to the peak metamorphism (M_{PR} to M_P) in quartzofeldspathic gneiss would have occurred between 1621 ± 14 Ma and 1581 ± 15 Ma (Fig. 10c).

The significance of 1479–1377 Ma (CD_G-IV) age population is not clear, as these domains do not show any relation with other monazite domains and tectonic fabrics (Fig. 9c). However, the higher abundance of Sm and Gd in the CD_G-IV domain ($\text{Sm}_2\text{O}_3 = 3\text{--}4\%$ and $\text{Gd}_2\text{O}_3 = 0.60\text{--}3.27\%$; Fig. S8d) indicating the breakdown of garnet and releasing the MREE's and HREE's, leaving monazite domains enriched in these elements. Therefore, we speculate that 1438 ± 25 Ma age (MSWD = 0.73; $n = 11$) obtained from the CD_G-IV domain represents the timing of post-peak re-equilibration and the stabilization of sillimanite needles in the matrix (Fig. 10b). The domain CD_G-V with relatively low Sm + Gd ($\text{Sm}_2\text{O}_3 = 2\text{--}4\%$ and $\text{Gd}_2\text{O}_3 = 0.6\text{--}1.57\%$) is seen overgrowing CD_G-III, IV (Fig. 9b). The Neoproterozoic ages from this domain 903–819 Ma are similar to those ages recorded from the pelites of KSB, which may correspond to a localized D_{3G} shearing event (Figs. 2f, 10b).

Geodynamic implications

The results obtained in this study, together with previous data from the Ongole and Vinjamuru Domains (Gupta et al. 1984; Dobmeier et al. 2006; Dharma Rao and Reddy 2009; Ravikant et al. 2010; Vijaya Kumar et al. 2010; Dharma Rao et al. 2011a; Chatterjee et al. 2016; Sarkar and Schenk 2016; Hrushikesh et al. 2019), and Napier–Rayner Complex of East Antarctica (Grew and Manton 1979; Clarke 1988; Grew et al. 2001; Harley 2003; Halpin et al. 2005, 2007; Harley et al. 2013), suggest the following regional and geodynamic implications (Fig. S9). The oldest Archean dates of 2785–2445 Ma and Mesoproterozoic high-grade metamorphic events (1659–1575 Ma and 1631–1533 Ma) are recorded from the EGMB quartzofeldspathic gneisses (Fig. 9), which are similar to those documented in the Ongole Domain (~ 2600–2400 Ma and ~ 1650–1550 Ma; Simmat and Raith 2008; Henderson et al. 2014). This suggests the possible westward extension of the Ongole domain. Henderson et al. (2014) performed detrital zircon analysis from the Ongole Domain and demonstrated that the Neoproterozoic ages were possibly derived from the Napier complex of East Antarctica, which indicates the timing of

UHT metamorphism in the Oygarden Group (Clarke 1988; Asami et al. 2002). These authors also postulated that the formation of the Ongole Domain occurred in the near vicinity of the Napier Complex during Late Paleoproterozoic to Early Mesoproterozoic (Henderson et al. 2014). This inference is based on the sporadically preserved similar ages in the Rayner–Napier complex on account of felsic magmatism and UHT metamorphism (Kelly et al. 2002; Halpin et al. 2005, 2013; Horie et al. 2016). Therefore, our new data from the Khammam region support that the Neoproterozoic components in the Ongole Domain were possibly derived from the Rayner–Napier Complex of East Antarctica.

Further, the high-T metamorphic events recorded in the quartzofeldspathic gneiss (1659–1575 Ma and 1631–1533 Ma; Fig. 9) are temporally consistent with partial melting (1620–1600 Ma) and crustal reworking (1550–1540 Ma) events identified in the Ongole Domain (cf. Sarkar et al. 2014, Sarkar et al. 2015). According to Sarkar et al. (2015), the heat required for the high-T and UHT metamorphism would have been derived from the magmatic underplating beneath the Ongole magmatic arc in a subduction zone setting. The 1479–1377 Ma tectonic overprint in the quartzofeldspathic gneiss may be related to the terminal rifting of the Columbia supercontinent that led to the dispersal of continental blocks with simultaneous alkaline magmatism in southeastern India and East Antarctica (Fig. S9; Dobmeier and Raith 2003; Simmat and Raith 2008; Upadhyay 2008; Dharma Rao et al. 2011a; Sarkar et al. 2015; Subramanyam et al. 2016; Sain et al. 2017). However, due to the absence of alkaline magmatism within the Khammam region, the significance of the Late Mesoproterozoic (1438 ± 25 Ma) event is unclear.

In contrast, KSB metapelites experienced Late Mesoproterozoic metamorphic episodes at 1253–1196 Ma and 1178–1102 Ma (Fig. 10). The tectonic scenario of these metamorphic events can be best explained as a result of emplacement of the Chimalpahad Anorthosite Complex (Fig. 1b; Sm–Nd whole-rock age: 1300–1100 Ma; Dharma Rao et al. 2011b) that favored an increase in temperature. Such evidence of arc magmatism and associated metamorphism indicates prolonged subduction in the Khammam region. Further, it has been interpreted that the tectonothermal events between 1253 and 1102 Ma are due to protracted accretion between SE India and East Antarctica during the formation of the Rodinia supercontinent (Fig. S9). This conclusion is based on the development of compressional fabrics and high-T metamorphism in the KSB metapelites (Figs. 10 and S9). On integrating published age data from the Vinjamuru domain metapelites (1650–1550 Ma, 1500–1400 Ma, and 1380–1250 Ma; Hrushikesh et al. 2019), it becomes evident that the KSB metapelites have experienced distinct metamorphic history (Figs. 10 and S9). The disparity in the tectonothermal histories reveals that the KSB, Vinjamuru

Domain, and Ongole Domain evolved distinctly during Late Paleoproterozoic to Late Mesoproterozoic (Fig. S9).

The youngest metamorphic event (903–813 Ma; this study) retrieved from the monazite rims not only attributed to the timing of N–S directed shearing (this study; Figs. 2f, 10 and S9) but also demarcate the shearing event in the adjacent Ongole and Vinjamuru domains (Sarkar et al. 2014; Hrushikesh et al. 2019). On a regional scale, this Neoproterozoic shearing event appears contemporary with the 870–780 Ma sinistral shearing and anatexis in the Eastern Indian Tectonic Zone (EITZ) that formed during the southward movement of India after its collision with East Antarctica at ~1000 Ma in the Rodinia assembly (Chatterjee et al. 2010). Therefore, we assume that the shearing event related to the formation of EITZ extends westward into the Ongole Domain and NKSB (Figs. 10 and S9). Nevertheless, such a presumption requires a detailed petrochronological analysis to determine the effect of 870–780 Ma anatexis in various crustal terranes in southeastern India.

Conclusions

Pressure–temperature–time estimates, described in this study using an integrated approach involving microtextural relationships, conventional thermobarometry, pseudosection modeling, and monazite dating, provide deeper insights into the polycyclic tectonothermal evolution of southeastern India. The studied EGMB quartzofeldspathic gneisses in the Khammam region have experienced high-T metamorphism with the peak P – T conditions of 7.9–8.1 kbar and 790–810 °C. In contrast, the garnet–kyanite schists investigated from the KSB witnessed MP–HT conditions of 7.4–7.8 kbar and 600–640 °C. The high-T metamorphism of quartzofeldspathic gneisses (EGMB component) is explained by the partial melting beneath the crust during the formation of the Ongole Domain at ca. 1659–1533 Ma. Whereas, the MP–HT metamorphism in KSB pelites (1178–1102 Ma) was related to the collision between Indian and East Antarctica in Rodinia assembly. We suggest that the Neoproterozoic components retrieved from the quartzofeldspathic gneisses were probably derived from the Napier Complex of East Antarctica. All the lithologies in the Khammam region witnessed a Neoproterozoic shearing event (903–813 Ma), which is possibly contemporaneous with the formation of EITZ and might have developed as a result of post-collisional (c. 1.0 Ga) adjustments between India and East Antarctica after the Rodinia assembly. Based on the absence of this shearing event in EDC rocks, we suggest that the effect of this shearing is terminated within the KSB. Therefore, the Khammam region with protracted tectonothermal history (2785–2445 Ma and 1659–813 Ma) is an analogue for a hot collision zone, which evolved as a composite terrane during meso- to neoproterozoic time.

Acknowledgements The Science and Engineering Research Board (SERB), India (SR/FTP/ES-5/2014), and the seed-grant of the Indian Institute of Technology Bombay (13IRCCSG025) jointly provided funding for this work. HH acknowledges the financial support provided by the University Grants Commission (UGC), New Delhi. Mineral analyses and monazite dating were carried out using the DST-sponsored CAMECA SX-Five electron microprobe housed in the Department Earth Sciences, IIT Bombay. Diptiranjan Mall for his assistance during the fieldwork, and Javed M Shaikh and Suranjan Ghosh for their help in EPMA mineral analyses. We appreciate S. C. Patel for fruitful discussions in various stages of this research work, and Nilanjan Chatterjee and Takamoto Okudaira for helpful comments on an initial version of the manuscript. J. A. D. Connolly is thanked for his help with phase equilibria modeling. We thank two anonymous reviewers for their constructive and insightful comments. Editorial efforts and valuable comments by Daniela Rubatto and Othmar Müntener helped to substantially improve the presentation of this manuscript.

References

- Asami M, Suzuki K, Grew ES (2002) Chemical Th–U–total Pb dating by electron microprobe analysis of monazite, xenotime and zircon from the Archean Napier Complex, East Antarctica: evidence for ultra-high-temperature metamorphism at 2400 Ma. *Precambrian Res* 114(3–4):249–275
- Bea F, Montero P (1999) Behavior of accessory phases and redistribution of Zr, REE, Y, Th, and U during metamorphism and partial melting of metapelites in the lower crust: an example from the Kinzigite Formation of Ivrea-Verbano NW, Italy. *Geochim Cosmochim Acta* 63(7–8):1133–1153
- Beaumont C, Ellis S, Hamilton J, Fullsack P (1996) Mechanical model for subduction-collision tectonics of Alpine-type compressional orogens. *Geology* 24(8):675
- Bhattacharya A, Mohanty L, Maji A, Sen S, Raith M (1992) Non-ideal mixing in the phlogopite-annite binary: constraints from experimental data on Mg–Fe partitioning and a reformulation of the biotite-garnet geothermometer. *Contrib Miner Petrol* 111(1):87–93
- Brown D, Spadea P, Puchkov V, Alvarez-Marron J, Herrington R, Willner A, Hetzel R, Gorozhanina Y, Juhlin C (2006) Arc-continent collision in the Southern Urals. *Earth Sci Rev* 79(3–4):261–287
- Cawood PA, Buchan C (2007) Linking accretionary orogenesis with supercontinent assembly. *Earth Sci Rev* 82(3–4):217–256
- Chatterjee N, Banerjee M, Bhattacharya A, Maji A (2010) Monazite chronology, metamorphism–anatexis and tectonic relevance of the mid-Neoproterozoic Eastern Indian Tectonic Zone. *Precambrian Res* 179(1–4):99–120
- Chatterjee C, Vadlamani R, Kaptan OP (2016) Paleoproterozoic Cordilleran-style accretion along the south eastern margin of the eastern Dharwar craton: evidence from the Vinjamuru arc terrane of the Krishna orogen, India. *Lithos* 263:122–142
- Clarke GL (1988) Structural constraints on the Proterozoic reworking of Archaean crust in the Rayner Complex, MacRobertson and Kemp Land coast, East Antarctica. *Precambrian Res* 40:137–156
- Connolly JA (2005) Computation of phase equilibria by linear programming: a tool for geodynamic modeling and its application to subduction zone decarbonation. *Earth Planet Sci Lett* 236(1–2):524–541
- Connolly JAD, Petrini K (2002) An automated strategy for calculation of phase diagram sections and retrieval of rock properties as a function of physical conditions. *J Metamorph Geol* 20:697–708
- Dahl PS, Hamilton MA, Jercinovic MJ, Terry MP, Williams ML, Frei R (2005) Comparative isotopic and chemical geochronometry of monazite, with implications for U–Th–Pb dating by electron microprobe: An example from metamorphic rocks of the eastern Wyoming Craton (USA). *Am Mineral* 90(4):619–638
- Deshmukh T, Prabhakar N, Bhattacharya A, Madhavan K (2017) Late Palaeoproterozoic clockwise *P–T* history in the Mahakoshal Belt, Central Indian Tectonic zone: implications for Columbia supercontinent assembly. *Precambrian Res* 298:56–78
- Dharma Rao CV, Reddy U (2009) Petrological and geochemical characterization of Proterozoic ophiolitic mélange, Nellore-Khammam schist belt, SE India. *J Asian Earth Sci* 36(4–5):261–276
- Dharma Rao CV, Santosh M, Wu Y-B (2011a) Mesoproterozoic ophiolitic mélange from the SE periphery of the Indian plate: U–Pb zircon ages and tectonic implications. *Gondwana Res* 19(2):384–401
- Dharma Rao CV, Windley B, Choudhary A (2011b) The Chimalpahad anorthosite Complex and associated basaltic amphibolites, Nellore Schist Belt, India: magma chamber and roof of a Proterozoic island arc. *J Asian Earth Sci* 40(5):1027–1043
- Diener J, Powell R (2010) Influence of ferric iron on the stability of mineral assemblages. *J Metamorph Geol* 28(6):599–613
- Diener JFA, White RW, Powell R (2008) Granulite facies metamorphism and subsolidus fluid-absent reworking, Strangways Range, Arunta Block, central Australia. *J Metamorph Geol* 26(6):603–622
- Dobmeier CJ, Raith MM (2003) Crustal architecture and evolution of the Eastern Ghats Belt and adjacent regions of India. *Geol Soc Lond Spec Publ* 206(1):145–168
- Dobmeier C, Lütke S, Hammerschmidt K, Mezger K (2006) Emplacement and deformation of the Vinukonda meta-granite (Eastern Ghats, India)—implications for the geological evolution of peninsular India and for Rodinia reconstructions. *Precambrian Res* 146(3–4):165–178
- Dumond G, Goncalves P, Williams M, Jercinovic M (2015) Monazite as a monitor of melting, garnet growth and feldspar recrystallization in continental lower crust. *J Metamorph Geol* 33(7):735–762
- England PC, Thompson AB (1984) Pressure–temperature–time paths of regional metamorphism I. Heat transfer during the evolution of regions of thickened continental crust. *J Petrol* 25(4):894–928
- Ferry JT, Spear F (1978) Experimental calibration of the partitioning of Fe and Mg between biotite and garnet. *Contrib Miner Petrol* 66(2):113–117
- Ganguly J, Saxena SK (1984) Mixing properties of aluminosilicate garnets: constraints from natural and experimental data, and applications to geothermo-barometry. *Am Miner* 69(1–2):88–97
- Grew ES, Manton WI (1979) Archean rocks in Antarctica: 2.5-billion-year uranium-lead ages of pegmatites in Enderby Land. *Science* 206(4417):443–445
- Grew ES, Suzuki K, Asami M (2001) CHIME ages of xenotime, monazite and zircon from beryllium pegmatites in the Napier Complex, Khmara Bay, Enderby Land, East Antarctica. *Polar Geosci* 14:99–118
- Groppo C, Rubatto D, Rolfo F, Lombardo B (2010) Early Oligocene partial melting in the main central thrust zone (Arun valley, eastern Nepal Himalaya). *Lithos* 118(3–4):287–301
- Gupta J, Pandey B, Chabria T, Banerjee D, Jayaram KV (1984) Rb–Sr geochronological studies on the granites of Vinukonda and Kanigiri, Prakasam district, Andhra Pradesh, India. *Precambrian Res* 26(2):105–109
- Hackler RT, Wood BJ (1989) Experimental determination of Fe and Mg exchange between garnet and olivine and estimation of Fe–Mg mixing properties in garnet. *Am Miner* 74(9–10):994–999
- Halpin J, Gerakiteys C, Clarke G, Belousova E, Griffin W (2005) In-situ U–Pb geochronology and Hf isotope analyses of the Rayner Complex, east Antarctica. *Contrib Miner Petrol* 148(6):689–706

- Halpin JA, White R, Clarke G, Kelsey D (2007) The Proterozoic P-T-t evolution of the Kemp Land coast, East Antarctica; constraints from Si-saturated and Si-undersaturated metapelites. *J Petrol* 48(7):1321–1349
- Halpin JA, Daczko NR, Clarke GL, Murray KR (2013) Basin analysis in polymetamorphic terranes: an example from east Antarctica. *Precambrian Res* 231:78–97
- Hari Prasad B, Okudaira T, Divi R, Yoshida M (1999) Structural features of the Archean Nellore-Khammam Schist Belt, Southeast India. *J Geosci Osaka City Univ* 42:227–235
- Hari Prasad B, Okudaira T, Hayasaka Y, Yoshida M, Divi R (2000) Petrology and geochemistry of amphibolites from the Nellore-Khammam schist belt, SE India. *J Geol Soc India* 56(1):67–78
- Harley S (2003) Archaean-Cambrian crustal development of East Antarctica: metamorphic characteristics and tectonic implications. *Geol Soc Lond Spec Publ* 206(1):203–230
- Harley SL, Fitzsimons IC, Zhao Y (2013) Antarctica and supercontinent evolution: historical perspectives, recent advances and unresolved issues. *Geol Soc Lond Spec Publ* 383(1):1–34
- Harris N, Santosh M, Taylor P (1994) Crustal evolution in South India: constraints from Nd isotopes. *J Geol* 102(2):139–150
- Henderson B, Collins AS, Payne J, Forbes C, Saha D (2014) Geologically constraining India in Columbia: the age, isotopic provenance and geochemistry of the protoliths of the Ongole Domain, Southern Eastern, Ghats India. *Gondwana Res* 26(3–4):888–906
- Henry DJ, Guidotti CV, Thomson JA (2005) The Ti-saturation surface for low-to-medium pressure metapelitic biotites: Implications for geothermometry and Ti-substitution mechanisms. *Am Miner* 90(2–3):316–328
- Hoisch TD (1990) Empirical calibration of six geobarometers for the mineral assemblage quartz+ muscovite+ biotite+ plagioclase+ garnet. *Contrib Miner Petrol* 104(2):225–234
- Holdaway M (2000) Application of new experimental and garnet Margules data to the garnet-biotite geothermometer. *Am Miner* 85(7–8):881–892
- Holdaway MJ (2001) Recalibration of the GASP geobarometer in light of recent garnet and plagioclase activity models and versions of the garnet-biotite geothermometer. *Am Mineral* 86(10):1117–1129
- Holland T, Powell R (1998) An internally consistent thermodynamic data set for phases of petrological interest. *J Metamorph Geol* 16(3):309–343
- Holland TJB, Powell R (2011) An improved and extended internally consistent thermodynamic dataset for phases of petrological interest, involving a new equation of state for solids. *J Metamorph Geol* 29(3):333–383
- Horie K, Hokada T, Motoyoshi Y, Shiraishi K, Hiroi Y, Takehara M (2016) U-Pb zircon geochronology in the western part of the Rayner Complex, East Antarctica. *J Mineral Petrol Sci* 111(2):104–117
- Hrushikesh H, Prabhakar N, Bhattacharya A (2019) Mesoproterozoic P-T-t-d history in the Vinjamuru domain, Nellore schist belt (SE India), and implications for SE India-East Antarctica correlation. *Precambrian Res* 327:273–295
- Jamieson RA, Beaumont C, Nguyen M, Lee B (2002) Interaction of metamorphism, deformation and exhumation in large convergent orogens. *J Metamorph Geol* 20(1):9–24
- Jercinovic MJ, Williams ML (2005) Analytical perils (and progress) in electron microprobe trace element analysis applied to geochronology: Background acquisition, interferences, and beam irradiation effects. *Am Miner* 90(4):526–546
- Jercinovic MJ, Williams ML, Allaz J, Donovan JJ (2012) Trace analysis in EPMA. In IOP conference series: materials science and engineering, 2012 Mar 7, vol 32, no 1, p 012012. IOP Publishing
- Kelly N, Clarke G, Fanning C (2002) A two-stage evolution of the Neoproterozoic Rayner Structural Episode: new U-Pb sensitive high resolution ion microprobe constraints from the Oygarden Group, Kemp Land, East Antarctica. *Precambrian Res* 116(3–4):307–330
- Keppeler H, Wyllie PJ (1990) Role of fluids in transport and fractionation of uranium and thorium in magmatic processes. *Nature* 348(6301):531–533
- Kluth CF, Coney PJ (1981) Plate tectonics of the Ancestral Rocky Mountains. *Geology* 9(1):10
- Knoper M, Armstrong R, Andreoli M, Ashwal L (2000) The Steenkampskraal monazite vein: a subhorizontal stretching shear zone indicating extensional collapse of Namaqualand at 1033 Ma? *J Afr Earth Sci* 31(1):38–38
- Korhonen F, Brown M, Clark C, Bhattacharya S (2013) Osumilite-melt interactions in ultrahigh temperature granulites: phase equilibria modelling and implications for the P-T-t evolution of the Eastern Ghats Province, India. *J Metamor Geol* 31(8):881–907
- Kovach V, Simmat R, Rickers K, Berezhnaya N, Salnikova E, Dobmeier C, Raith M, Yakovleva S, Kotov A (2001) The Western Charnokite Zone of the Eastern Ghats Belt, India—an independent Crustal Province of Late Archaean (2.8 Ga) and Palaeoproterozoic (1.7–1.6 Ga) Terrains. *Gondwana Res* 4(4):666–667
- Kumar R, Okudaira T, Tani Y, Hari Prasad B, Divi R, Yoshida M (1999) Structural Features around the Archean-Proterozoic Terrain Boundary in Khammam District, South India. *J Geosci Osaka City Univ* 42:227–235
- Kumar R, Okudaira T, Yoshida M (2000) Neoproterozoic deformation at a boundary zone between the Nellore-Khammam Schist Belt and Pakhal Basin, SE India: strain analysis of deformed pebbles. *Gondwana Res* 3(3):349–359
- La Roche RS, Gervais F, Tremblay A, Crowley JL, Ruffet G (2015) Tectono-metamorphic history of the eastern Taureau shear zone, Mauricie area, Québec: implications for the exhumation of the mid-crust in the Grenville Province. *Precambrian Res* 257:22–46
- Leelanandam C, Narsimha Reddy M (1988) Precambrian anorthosites from Peninsular India: problems and perspectives. *Indian J Geol* 60:111–136
- Ludwig KR (2003) Isoplot 3.00: a geochronological toolkit for Microsoft Excel. Berkeley Geochronology Center Special Publication 4:70
- Mahan K, Goncalves P, Williams M, Jercinovic MJ (2006) Dating metamorphic reactions and fluid flow: application to exhumation of high-P granulites in a crustal-scale shear zone, western Canadian Shield. *J Metamorph Geol* 24(3):193–217
- Merlet C (1992) Quantitative electron probe microanalysis: new accurate $\Phi(\rho z)$ description. *Electron microbeam analysis*. Springer, Berlin, pp 107–115
- Montel JM, Foret S, Veschambre M, Nicollet C, Provost A (1996) Electron microprobe dating of monazite. *Chem Geol* 131:37–53
- Narayananwami S (1966) Tectonics of the Cuddapah basin. *Geol Soc India* 7:33–50
- Newton R, Charlu T, Kleppa O (1980) Thermochemistry of the high structural state plagioclases. *Geochim Cosmochim Acta* 44(7):933–941
- Norris R, Koons P, Cooper A (1990) The obliquely-convergent plate boundary in the South Island of New Zealand: implications for ancient collision zones. *J Struct Geol* 12(5–6):715–725
- Okudaira T, Hamamoto T, Hari Prasad B, Rajneesh Kumar R (2001) Sm-Nd and Rb-Sr dating of amphibolite from the Nellore-Khammam schist belt, SE India: constraints on the collision of the Eastern Ghats terrane and Dharwar-Bastar craton. *Geol Mag* 138(4):495–498
- Palin RM, Weller OM, Waters DJ, Dyck B (2016) Quantifying geological uncertainty in metamorphic phase equilibria

- modelling; a Monte Carlo assessment and implications for tectonic interpretations. *Geosci Front* 7:591–607
- Prabhakar N (2013) Resolving poly-metamorphic Paleoproterozoic ages by chemical dating of monazites using multi-spectrometer U, Th and Pb analyses and sub-counting methodology. *Chem Geol* 347:255–270
- Rahimi G, Massonne HJ (2018) Pressure-temperature-time evolution of a Varsican garnet-bearing micaschist from the northeastern Fichtelgebirge, NW Bohemian Massif in central Europe. *Lithos* 316:366–384
- Ramam P, Murty V (1997) *Geology of Andhra Pradesh: Geological Society of India, India*
- Ravikant V (2010) Palaeoproterozoic (~1.9 Ga) extension and breakup along the eastern margin of the Eastern Dharwar Craton, SE India: New Sm–Nd isochron age constraints from anorogenic mafic magmatism in the Neoproterozoic Nellore greenstone belt. *J Asian Earth Sci* 37(1):67–81
- Rosenberg C, Handy M (2005) Experimental deformation of partially melted granite revisited: implications for the continental crust. *J Metamorph Geol* 23(1):19–28
- Saha D (2002) Multi-stage deformation in the Nallamalai Fold Belt, Cuddapah basin, South India—Implications for Mesoproterozoic tectonism along southeastern margin of India. *Gondwana Res* 5(3):701–719
- Sain A, Saha D, Joy S, Jelsma H, Armstrong R (2017) New SHRIMP age and microstructures from a deformed A-type Granite, Kanigiri, Southern India: constraining the Hiatus between orogenic closure and postorogenic rifting. *J Geol* 125(2):241–259
- Sangam N, Pavanaguru R (2013) Geology of Corundum Occurrences in Parts of Khammam Schist Belt. *Int J Sci Res Publ* 3(2):1–3
- Sarkar T, Schenk V (2014) Two-stage granulite formation in a Proterozoic magmatic arc (Ongole domain of the Eastern Ghats Belt, India): Part 1. Petrology and pressure–temperature evolution. *Precambrian Res* 255:485–509
- Sarkar T, Schenk V (2016) Early Mesoproterozoic (1.6–1.5 Ga) granulite facies events in the Ongole domain: geodynamic significance and global correlation. *J Metamorph Geol* 34(8):765–784
- Sarkar T, Schenk V, Berndt J (2015) Formation and evolution of a Proterozoic magmatic arc: geochemical and geochronological constraints from meta-igneous rocks of the Ongole domain, Eastern Ghats Belt, India. *Contrib Mineral Petrol* 169(1):5
- Sawyer E (2001) Melt segregation in the continental crust: distribution and movement of melt in anatexitic rocks. *J Metamorph Geol* 19(3):291–309
- Sharma R (2009) *Cratons and fold belts of India*. Springer, Berlin
- Sheth HC, Choudhary AK, Bhattacharyya S, Cucciniello C, Laishram R, Gurav T (2011) The Chogat-Chamardi subvolcanic complex, Saurashtra, northwestern Deccan Traps: geology, petrochemistry, and petrogenetic evolution. *J Asian Earth Sci* 41(3):307–324
- Simmat R, Raith MM (2008) U–Th–Pb monazite geochronometry of the Eastern Ghats Belt, India: timing and spatial disposition of poly-metamorphism. *Precambrian Res* 162(1–2):16–39
- Spear FS, Florence FP (1992) Thermobarometry in granulites: pitfalls and new approaches. *Precambrian Res* 55(1–4):209–241
- Spear FS, Pyle JM (2010) Theoretical modeling of monazite growth in a low-Ca metapelite. *Chem Geol* 273(1–2):111–119
- Spear FS, Pyle JM, Cherniak D (2009) Limitations of chemical dating of monazite. *Chem Geol* 266(3–4):218–230
- Sarkar T, Schenk V, Appel P, Berndt J, Sengupta P (2014) Two-stage granulite formation in a Proterozoic magmatic arc (Ongole domain of the Eastern Ghats Belt, India): Part 2. LA-ICP-MS zircon dating and texturally controlled in-situ monazite dating. *Precambrian Res* 255:467–484
- Subramanyam K, Santosh M, Yang Q-Y, Zhang Z-m, Balam V, Reddy U (2016) Mesoproterozoic island arc magmatism along the south-eastern margin of the Indian Plate: evidence from geochemistry and zircon U–Pb ages of mafic plutonic complexes. *J Asian Earth Sci* 130:116–138
- Suzuki K, Adachi M (1991) Precambrian provenance and Silurian metamorphism of the Tsubonosawa paragneiss in the South Kitakami terrane, Northeast Japan, revealed by the chemical Th–U–total Pb isochron ages of monazite, zircon and xenotime. *Geochem J* 25(5):357–376
- Tinkham DK, Zuluaga CA, Stowell HH (2001) Metapelite phase equilibria modeling in MnNCKFMASH: the effect of variable Al₂O₃ and MgO/(MgO+ FeO) on mineral stability. *Geol Mater Res* 3(1):1–42
- Upadhyay D (2008) Alkaline magmatism along the southeastern margin of the Indian shield: implications for regional geodynamics and constraints on craton–Eastern Ghats Belt suturing. *Precambrian Res* 162(1–2):59–69
- Vernon R (1978) Porphyroblast-matrix microstructural relationships in deformed metamorphic rocks. *Geol Rundsch* 67(1):288–305
- Vijaya Kumar K, Narsimha Reddy M, Leelanandam C (2006) Dynamic melting of the Precambrian mantle: evidence from rare earth elements of the amphibolites from the Nellore-Khammam schist belt, South India. *Contrib Miner Petrol* 152:243–256
- Vijaya Kumar K, Ernst W, Leelanandam C, Wooden J, Grove M (2010) First Paleoproterozoic ophiolite from Gondwana: geochronologic–geochemical documentation of ancient oceanic crust from Kandra SE, India. *Tectonophysics* 487(1–4):22–32
- Waldbaum D, Thompson J Jr (1968) Mixing properties of sanidine crystalline solutions: II. Calculations based on volume data. *Am Mineral J Earth Planet Mater* 53(11–12):2000–2017
- White R, Powell R, Clarke G (2002) The interpretation of reaction textures in Fe-rich metapelitic granulites of the Musgrave Block, central Australia: constraints from mineral equilibria calculations in the system K₂O–FeO–MgO–Al₂O₃–SiO₂–H₂O–TiO₂–Fe₂O₃. *J Metamorph Geol* 20(1):41–55
- White R, Powell R, Halpin J (2004) Spatially-focussed melt formation in aluminous metapelites from Broken Hill. *Aust J Metamorph Geol* 22(9):825–845
- White R, Powell R, Holland T, Johnson T, Green E (2014) New mineral activity–composition relations for thermodynamic calculations in metapelitic systems. *J Metamorph Geol* 32(3):261–286
- Whitney DL, Evans BW (2010) Abbreviations for names of rock-forming minerals. *Am Miner* 95(1):185–187
- Williams ML, Jercinovic MJ (2002) Microprobe monazite geochronology: putting absolute time into microstructural analysis. *J Struct Geol* 24(6–7):1013–1028
- Williams M, Jercinovic M, Goncalves P, Mahan K (2006) Format and philosophy for collecting, compiling, and reporting microprobe monazite ages. *Chem Geol* 225(1–2):1–15
- Wu CM (2017) Calibration of the garnet–biotite–Al₂SiO₅–quartz geobarometer for metapelites. *J Metamorph Geol* 35(9):983–998
- Xing L, Trail D, Watson EB (2013) Th and U partitioning between monazite and felsic melt. *Chem Geol* 358:46–53
- Zhao G, Cawood PA (1999) Tectonothermal evolution of the Mayuan Assemblage in the Cathaysia Block; implications for Neoproterozoic collision-related assembly of the South China Craton. *Am J Sci* 299(4):309–339
- Zhuang G, Najman Y, Guillot S, Roddaz M, Antoine P-O, Métais G, Carter A, Marivaux L, Solangi SH (2015) Constraints on the collision and the pre-collision tectonic configuration between India and Asia from detrital geochronology, thermochronology, and geochemistry studies in the lower Indus basin, Pakistan. *Earth Planet Sci Lett* 432:363–373